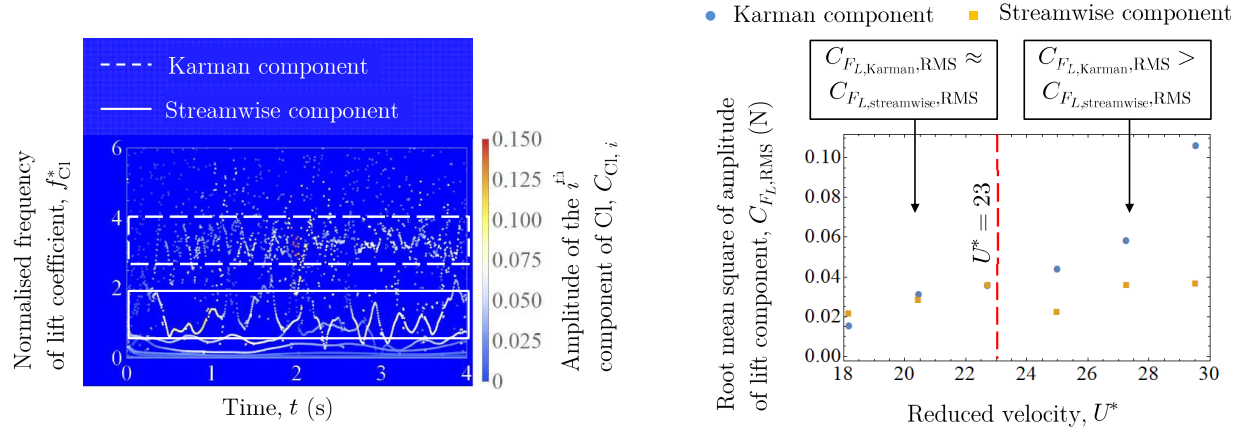


## 1 Graphical Abstract

### 2 Temporal Evolution of Lift in a Pure Cruciform System for Energy Harvesting

3 Ahmad Adzlan,Mohamed Sukri Mat Ali,Sheikh Ahmad Zaki Shaikh Salim



**4 Highlights**

**5 Temporal Evolution of Lift in a Pure Cruciform System for Energy Harvesting**

**6 Ahmad Adzlan,Mohamed Sukri Mat Ali,Sheikh Ahmad Zaki Shaikh Salim**

- 7** • Decomposition of the lift coefficient signal via ensemble empirical mode decomposition (EEMD) brings to the  
**8** fore the components of lift generated by the shedding of Karman and streamwise vortices, which in its original  
**9** form is observed as one non-monotonic lift signal in the streamwise vortex-induced vibration (SVIV) regime.
- 10** • Determination of phase lag between lift and cylinder displacement using Hilbert-Huang transform (HHT) reveals  
**11** evidence suggesting the existence of an initial branch for SVIV.
- 12** • Contribution to the total root-mean-square (RMS) lift amplitude from the shedding of both Karman and stream-  
**13** wise vortices suggest that we might be able to enlarge the RMS amplitude – and as a result harnessed power –  
**14** if we can redirect energy away from Karman vortices towards streamwise vortices, in the SVIV regime.

# <sup>15</sup> Temporal Evolution of Lift in a Pure Cruciform System for Energy <sup>16</sup> Harvesting

<sup>17</sup> Ahmad Adzlan<sup>a,b,\*</sup>, Mohamed Sukri Mat Ali<sup>a</sup> and Sheikh Ahmad Zaki Shaikh Salim<sup>a</sup>

<sup>18</sup> <sup>a</sup>Malaysia-Japan International Institute of Technology, Universiti Teknologi Malaysia, 54200 Kuala Lumpur, Malaysia

<sup>19</sup> <sup>b</sup>Faculty of Engineering, Universiti Malaysia Sarawak, 94300 Kota Samarahan, Sarawak, Malaysia

<sup>20</sup>

---

## <sup>21</sup> ARTICLE INFO

<sup>24</sup> **Keywords:**

<sup>25</sup> Vortex-induced vibration

<sup>26</sup> Vibration energy harvester

<sup>27</sup> CFD simulation

<sup>28</sup> Streamwise vorticity

<sup>29</sup> Ensemble empirical mode decompo-

<sup>30</sup> sition (EEMD)

<sup>31</sup> Hilbert transform

<sup>32</sup>

<sup>33</sup>

<sup>34</sup>

<sup>35</sup>

<sup>36</sup>

<sup>37</sup>

<sup>38</sup>

<sup>39</sup>

<sup>40</sup>

---

## ABSTRACT

We investigated the amplitude and frequency responses of a circular cylinder - strip plate cruciform system in the Reynolds number range  $1.1 \times 10^3 < Re < 14.6 \times 10^3$  numerically using the open source C++ library: OpenFOAM. We decomposed the cylinder displacement and lift time series from our numerical results into Hilbert transform-friendly signals using the ensemble empirical mode decomposition (EEMD) method. The mean phase lag obtained through Hilbert transform points to the existence of an initial branch-like state, with a phase lag of  $\approx 20$  deg. in the narrow region of  $U^*$  close to 18.2. Then, the mean phase lag jumps from  $\approx 20$  deg. to  $\approx 110$  deg. once  $U^*$  reaches 20.5, analogous to the transition to upper branch in a KVIV amplitude response curve. The instantaneous phase lag shows that SVIV is quasi-periodic up until  $U^* = 27.3$ . Between  $18.2 < U^* < 22.5$ , Karman vortex shedding contributes nearly as much as streamwise vortex shedding to the root-mean-square amplitude of total lift, while between  $25.0 \leq U^* \leq 29.5$ , the Karman component contribution is on average twice that of the streamwise component. These findings hint at the possibility to improve the power output of the harvester by a factor of two between  $18.28 < U^* < 22.5$  and by a factor of three between  $25.0 \leq U^* \leq 29.5$ , if we can unite the contribution to the root-mean-square amplitude of the total lift under a single vibration-driving mechanism: the shedding of streamwise vortex.

## <sup>41</sup> 1. Introduction

<sup>42</sup> Streamwise vortex-induced vibration (SVIV) is a type of vortex-induced vibration (VIV) driven by vortical struc-  
<sup>43</sup> tures whose vorticity vector points in the direction of the free stream. In recent decades, there have been efforts to  
<sup>44</sup> exploit the SVIV phenomenon from cruciform structures for energy harvesting, an example of which is given in Fig.

<sup>45</sup> 1. The literature on this subject can be broadly categorised into two groups: how the mechanical properties of the  
<sup>46</sup> oscillator (e.g., mass ratio, damping, etc.) affects the amplitude/frequency response of SVIV (Koide et al., 2009, 2013;  
<sup>47</sup> Nguyen et al., 2012) and how the minutiae of the flow field affect the force driving the vibration of the cylinder, i.e.  
<sup>48</sup> the fluid mechanical aspect of the system (Deng et al., 2007; Koide et al., 2017; Zhao and Lu, 2018).

<sup>49</sup> In the first focus area, researchers studied some permutation of the following method to convert the vibration into  
<sup>50</sup> electrical power. The method consists of a coil and magnet. The coil, which moves with the vibrating cylinder, creates  
<sup>51</sup> relative motion against the magnet, which is placed in the hollow of the coil (Koide et al., 2009). While investigating  
<sup>52</sup> the system at a Reynolds number in the order of  $Re \sim O(10^4)$ , Koide et al. (2009) showed that increased damping  
<sup>53</sup> due to energy harvesting reduces the maximum vibration amplitude close to a factor of 4. Amplitude reduction due to

---

\*Corresponding author

✉ aafkhairi@graduate.utm.my (A. Adzlan); sukri.kl@utm.my (M.S.M. Ali); sheikh.kl@utm.my (S.A.Z.S. Salim)  
ORCID(s): 0000-0003-0290-3185 (A. Adzlan)

increased total damping was also mentioned in Bernitsas et al. (2008); Bernitsas and Raghavan (2008); Bernitsas et al. (2009). Further investigation in Nguyen et al. (2012) revealed that damping not only affects the amplitude response of the cylinder but also narrows the synchronisation region between vortex shedding and cylinder vibration. Moreover, Nguyen et al. (2012) demonstrated a strong coupling between mass ratio and damping in determining both the width of the synchronisation region and the maximum amplitude response of the cylinder.

In the second focus area, investigators turned their attention to the details of the flow where streamwise vortex shedding occurs. One such study carefully shot motion pictures of the dye-injected flow (Koide et al., 2017) at Reynolds number in the order of  $Re \sim O(10^3)$ . A lower Reynolds number ( $Re$ ) reduces the amount of turbulence in the flow, allowing a clearer shot of the vortex structures. Their study also highlights the higher level of turbulence produced by the circular cylinder-strip plate cruciform in contrast to the twin circular cylinder cruciform, which diminishes the periodicity of vortex shedding. Although visually enlightening, this and other more qualitative studies contribute little towards improving our understanding of the relationship between vortex shedding and the resulting lift. Deng et al. (2007) demonstrated a way to overcome such a shortcoming.

In their study, Deng et al. (2007) examined the flow field of a twin circular cylinder cruciform using computational fluid dynamics (CFD). Their domain stretches  $28D$  in the streamwise direction,  $16D$  in the transverse direction and  $12D$  in the spanwise direction. They studied an  $Re$  range yet another order of magnitude smaller than that studied by Koide et al. (2017), possibly to get an even clearer visualisation of the vortical structures with less turbulence, and to ease computational requisites.

At a fixed  $Re = 150$ , streamwise vortices form even at a gap ratio of 2. This result differs quite strikingly from Koide et al. (2006, 2007), conducted at an  $Re$  twice the order of magnitude of Deng et al. (2007), an indication that the minimum gap ratio needed for the onset of streamwise varies with respect to  $Re$ .

They also observed that when the gap ratio  $G$ , which they denote as  $L/D$  in their paper, increases from 3 to 4, the maximum amplitude of the lift coefficient increases by almost threefold. This can be attributed quite easily to the current vortex pair shed by the upstream cylinder. The downstream cylinder immediately disturbs the pair shed from the upstream cylinder when  $G = 3$ . The lift coefficient increases by about a factor of 3 when this immediate disturbance diminishes at  $G = 4$ . The visualisation of three-dimensional (3D) vorticity isocontours enables us to quickly establish this link vis-à-vis the lift coefficient signal. The authors use of CFD made this possible.

A similar study in the order of magnitude  $Re \sim O(10^2)$  by Zhao and Lu (2018) particularly highlighted the immense utility of CFD as a tool to research SVIV or flow around a cruciform in general. They computed the sectional lift coefficient along the upstream cylinder, and the time history of this sectional lift coefficient revealed two different modes of vortex shedding, namely, parallel and K-shaped. They also paid attention to the local flow patterns that vary along the length of the upstream cylinder such as the trailing vortex flow, necklace vortex flow and flow in the small gap

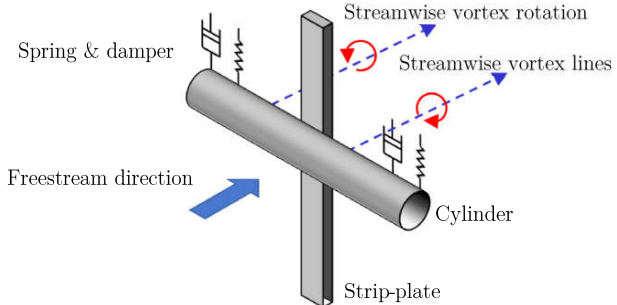


**Figure 1:** A schematic of the circular cylinder-strip plate cruciform system. Alternate shedding of the streamwise vortices create the alternating lift that drives the vibration of the cylinder.

(denoted as SG flow). The discontinuities in the phase angle of the sectional lift coefficient along the upstream cylinder seems to suggest the inadequateness of attributing the lift coefficient to streamwise vortex shedding alone, particularly when Karman vortex streamlines were also observed some distance away from the junction of the cruciform. Shirakashi et al. (1989) also made a similar observation in their experimental work. This leads us to hypothesise that the lift signal is more appropriately viewed as the streamwise-Karman vortex-induced composite lift signal. However, we could not find studies that took this viewpoint and worked out its implication on power generation in their investigation of SVIV.

The objectives of this study are thus threefold: (1) to take a closer look at the amplitude and frequency response of a circular cylinder-strip plate cruciform, especially in reduced velocity ( $U^*$ ) ranges where the transition from KVIV to SVIV occurs, (2) to demonstrate the compositeness of the lift signal of an SVIV system and establish the difference between the lift signal characteristics in the KVIV and SVIV regime and (3) to shed light on how the contribution from the Karman and streamwise components of lift changes as we increase  $U^*$  after the onset of SVIV and predict how much improvement in the power generation can be anticipated if we are able to unify the lift amplitude contributions due to Karman and streamwise vortex shedding. Here,  $U^* = U/f_n D$ , with  $U$ ,  $f_n$  and  $D$  being the freestream velocity, natural frequency of the system and the diameter of the circular cylinder respectively. The following §2 details the methodology we employ to conduct this study. We present and discuss our results in §4, §5, and §6. We describe our conclusions in §7.

## 2. Methodology

### 2.1. Problem geometry

The geometrical setup for this study builds on the work of Maruai et al. (2017, 2018) who studied both experimentally and numerically the FIM of a square cylinder with a downstream flat plate. Their simulation results are in good agreement with their own experiment, and with the experimental results of Kawabata et al. (2013), in the Reynolds number range  $3.6 \times 10^3 < Re < 12.5 \times 10^3$ . This is well within the Reynolds number studied in this work, i.e.

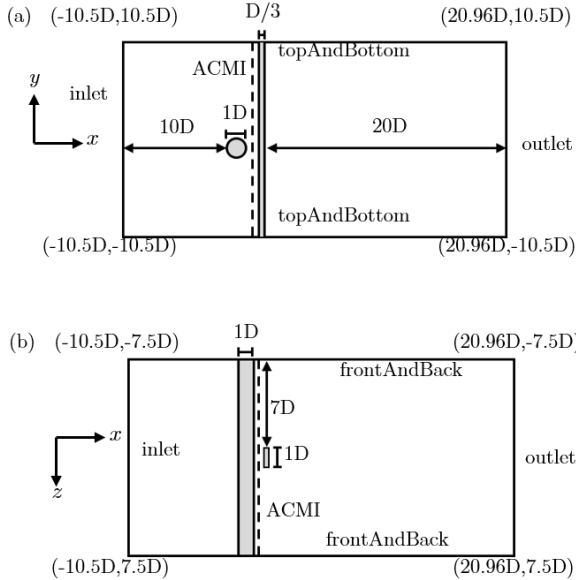


**Figure 2:** Problem geometry and coordinate system used. Figure 2a shows the side view of the simulation domain (viewed parallel to the freestream) while Fig. 2b shows the top view of the simulation domain (viewed perpendicular to the freestream). Note that the gap ratio  $G$  between the cylinder and the strip plate is  $0.16D$ , and the arbitrarily coupled mesh interface (ACMI) patch is located midway through the gap, i.e.,  $0.08D$  downstream from the trailing edge of the cylinder.

$$1.1 \times 10^3 < \text{Re} < 14.6 \times 10^3.$$

Our  $x - y$  plane fundamentally follows the dimensions used in Maruai et al. (2017, 2018), except for the cylinder shape, which in this study is circular, and the  $20D$  distance to the outlet is measured from the downstream face of the strip-plate. This is shown in Fig. 2. We chose the cylinder-plate gap  $G$  to be  $0.26D$ , as previous works have shown this gap size sustains the highest SVIV amplitude over the widest range of  $U^*$ , in comparison to other gap sizes.

As the problem geometry is explicitly three-dimensional (3D), the  $x - y$  plane is extruded in the  $z$  direction, thus obtaining a 3D domain. As can be seen in Fig. 2, the circular cylinder extends from  $z/D = 7.5$  to  $z/D = -7.5$ , while the strip-plate extends from  $-10.5$  to  $y/D = 10.5$ . The  $z$ -direction extent is set as  $z/D = \pm 7.5$  is already more than twice the spanwise reach of the streamwise vortex, thus sufficient for the vortices to materialise in our numerical solution. To compare, the spanwise extent of the numerical study by Deng et al. (2007), is  $z/D = \pm 6$  and the spanwise extents of experiments by Nguyen et al. (2012) and Koide et al. (2013) are  $z/D = \pm 5$ .

## 2.2. Numerical method

The objectives of our study necessitate the solution of the continuity, and 3D unsteady Reynolds averaged Navier-Stokes (3D URANS) equations. We achieve this by using OpenFOAM, an open-source computational fluid dynamics

<sup>122</sup> (CFD) platform written in C++. Specifically, we work to solve the following continuity and URANS equations.

$$\frac{\partial U_i}{\partial x_i} = 0, \quad (1)$$

$$\frac{\partial U_i}{\partial t} + U_j \frac{\partial U_i}{\partial x_j} = -\frac{1}{\rho} \frac{\partial P}{\partial x_i} + \frac{\partial}{\partial x_j} \left( 2\nu S_{ij} - \overline{u'_j u'_i} \right). \quad (2)$$

<sup>123</sup> The symbols  $U$ ,  $x$ ,  $t$ ,  $\rho$ ,  $P$ ,  $\nu$ ,  $S$ , and  $u'$  are the mean component of velocity, spatial component, time density,  
<sup>124</sup> pressure, kinematic viscosity, mean strain rate and the fluctuating component of velocity, respectively. The mean  
<sup>125</sup> strain rate  $S_{ij}$  is given by

$$S_{ij} = \frac{1}{2} \left( \frac{\partial U_i}{\partial x_j} + \frac{\partial U_j}{\partial x_i} \right). \quad (3)$$

<sup>126</sup> This study employs the Spalart-Allmaras turbulence model to approximate the Reynolds stress tensor  $\tau_{ij} = \overline{u'_j u'_i}$ .  
<sup>127</sup> This turbulence model has been shown to produce results that agree reasonably well with experiments in similar flow-  
<sup>128</sup> induced motion (FIM) studies (Ding et al., 2015a,b). We use the Boussinesq approximation to relate the Reynolds  
<sup>129</sup> stress tensor to the mean velocity gradient

$$\tau_{ij} = 2\nu_T S_{ij}, \quad (4)$$

<sup>130</sup> where  $\nu_T$  represents the kinetic eddy viscosity.  $\nu_T$  is, in turn, a function of  $\tilde{\nu}$  and  $f_{\nu 1}$ , while  $f_{\nu 1}$  is a function of  $\chi$  and  
<sup>131</sup>  $c_{\nu 1}$ , and  $\chi$  a function of  $\tilde{\nu}$  and  $\nu$ , as shown in Eq. 5.

$$\nu_T = \tilde{\nu} f_{\nu 1}, \quad (5a)$$

$$f_{\nu 1} = \frac{\chi^3}{\chi^3 + c_{\nu 1}^3}, \quad (5b)$$

$$\chi = \frac{\tilde{\nu}}{\nu}. \quad (5c)$$

<sup>132</sup> Here,  $\tilde{\nu}$  serves to mediate the turbulence model and dictates how  $\tilde{\nu}$  is conserved.

$$\frac{\partial \tilde{v}}{\partial t} + U_j \frac{\partial \tilde{v}}{\partial x_j} = c_{b1} \tilde{S} \tilde{v} - c_{w1} f_w \left( \frac{\tilde{v}}{D} \right)^2 + \frac{1}{\sigma} \left\{ \frac{\partial}{\partial x_j} \left[ (\nu + \tilde{v}) \frac{\partial \tilde{v}}{\partial x_j} \right] c_{b2} \frac{\partial \tilde{v}}{\partial x_i} \frac{\partial \tilde{v}}{\partial x_i} \right\} \quad (6)$$

<sup>133</sup>  $c_{b1}$ ,  $c_{b2}$ , and  $c_{\nu 1}$  are constant with values 0.1335, 0.622 and 7.1 respectively.  $c_{w1}$  is given by

$$c_{w1} = \frac{c_{b1}}{\kappa} + \frac{1 + c_{b2}}{\sigma}, \quad (7)$$

<sup>134</sup> where additional constants  $\kappa$  and  $\sigma$  are 0.41 and 2/3 respectively.  $f_w$ , on the other hand, is given by

$$f_w = g \left( \frac{1 + c_{w3}^6}{g^6 + c_{w3}} \right)^{\frac{1}{6}}. \quad (8)$$

<sup>135</sup> Here,  $c_{w3} = 2$  while  $g$  is given by

$$g = r + c_{w2} (r^6 - r), \quad (9)$$

<sup>136</sup> where  $r$  is

$$r = \min \left( \frac{\tilde{v}}{\tilde{S} \kappa^2 d^2}, 10 \right), \quad (10)$$

<sup>137</sup> Additionally,  $\tilde{S}$  is

$$\tilde{S} = \Omega + \frac{\tilde{v}}{\kappa^2 d^2} f_{\nu 2}, \quad (11)$$

<sup>138</sup> where  $\Omega$  and  $d$  are the magnitude of vorticity and the distance from the mesh nodes to the nearest wall, respectively.

<sup>139</sup> Finally,  $f_{v2}$  is

$$f_{v2} = 1 - \frac{\chi}{1 + \chi f_{v1}}. \quad (12)$$

<sup>140</sup> We solve these equations numerically using the PIMPLE algorithm, which combines the transient solver PISO with  
<sup>141</sup> the steady-state solver SIMPLE for improved numerical stability.

### <sup>142</sup> 2.3. Dynamic mesh motion

<sup>143</sup> In this study, the cylinder in VIV moves perpendicular to the free stream direction. The motion unavoidably  
<sup>144</sup> distorts the mesh around it, degrading important mesh metrics such as non-orthogonality and skewness. However, we  
<sup>145</sup> can diffuse the mesh deformation to the neighbouring nodes as per the following Laplace equation,

$$\nabla \cdot (\gamma \nabla u) = 0. \quad (13)$$

<sup>146</sup> Here,  $u$  represents the mesh deformation velocity and  $\gamma$  is displacement diffusion. We chose  $\gamma = 1/l^2$ , where  $l$  is the cell  
<sup>147</sup> centre distance to the nearest cylinder edges. We implement the GAMG linear solver with the Gauss-Seidel smoother to  
<sup>148</sup> solve Eq. 13. The dynamic mesh algorithm then updates the mesh node positions according to the following equation.

$$x_{\text{new}} = x_{\text{old}} + u \Delta t \quad (14)$$

<sup>149</sup> The solver resumes the solution of Eqs. 1 and 2 once the mesh node positions are updated.

<sup>150</sup> Another dynamic mesh handling technique used in this study is the arbitrarily coupled mesh interface (ACMI) that  
<sup>151</sup> allows non-conforming meshes to slide over another, thus preserving the mesh quality around a moving object. The  
<sup>152</sup> tiny gap between the cylinder and strip-plate, limits our ability to diffuse the mesh deformation to the surrounding  
<sup>153</sup> space. ACMI is thus implemented at the centre of the gap between the circular cylinder and the strip-plate, as shown in  
<sup>154</sup> Fig. 2, to circumvent this problem. This method has been successfully implemented in the works of Ding et al. (2015b);  
<sup>155</sup> Zhang et al. (2018), preserving the quality of their mesh and controlling their Courant-Friedrichs-Lowy (CFL) number.

### <sup>156</sup> 2.4. Open flow channel experiment

<sup>157</sup> We set up an experimental rig to validate our numerical results in the vicinity of reduced velocity  $U^* = 22.7$ . We  
<sup>158</sup> chose  $U^* = 22.7$  because that value of  $U^*$  is where the vibration-driving mechanism is known to transit from Karman

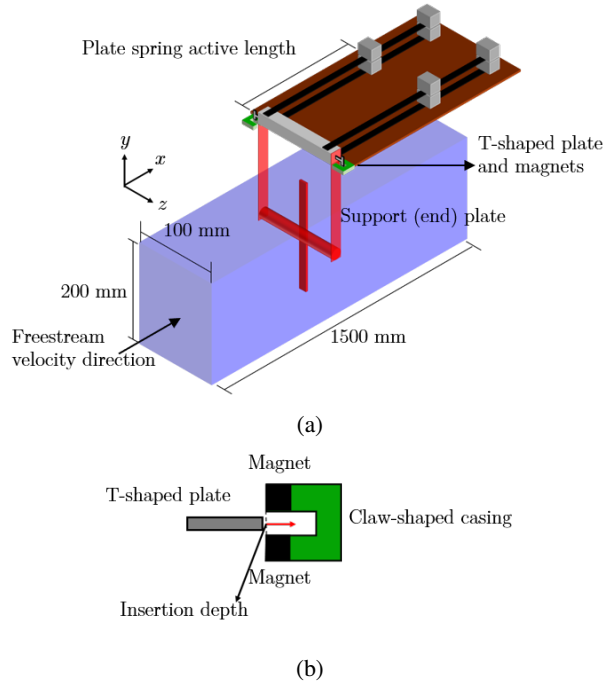


**Figure 3:** A schematic of our experimental setup. Figure 3a presents a 3D schematic of the experimental rig while Fig. 3b shows an enlarged schematic of the damping system.

159 to streamwise vortex shedding (Koide et al., 2013). The experimental rig consists of a closed-loop open channel circuit  
 160 based on the water tunnel used by Nguyen et al. (2012), shown in Fig. 3. The cross-section of our test section is a  
 161 square with sides 100 mm in length. The test section is 1500 mm long.

162 The system for providing elastic support and damping to the circular cylinder follows closely those used by Kawa-  
 163 bata et al. (2013) and Koide et al. (2013, 2017), which can be summarised as follows. The stiffness coefficient  $k$  of  
 164 the plate spring is determined through a simple weight versus displacement test (Sun et al., 2016), at various active  
 165 lengths of the spring. This provides a calibration curve of stiffness coefficient,  $k$  against plate spring length,  $l$ . We can  
 166 then adjust the length of the plate spring to obtain the desired value for  $k$ .

167 On the other hand, the damping of the system is adjusted using T-shaped aluminium plates fixed at either end of  
 168 the cylinder endplate, and a pair of neodymium magnets contained in a claw-shaped casing. The further the T-shaped  
 169 plate is pushed into the opening of the claw, the denser the magnetic field it needs to cut through during motion, thus  
 170 dissipating more energy. We then calibrate the damping produced at various depths at which the T-shaped plate is  
 171 pushed into the casing, via free-decay tests of the cylinder in still water. The procedure for conducting free-decay tests  
 172 are detailed in Raghavan (2007).

173 Flow inside the open channel is driven by a 3.728 kW (5 hp) centrifugal pump, controlled using a voltage controller.  
 174 The input voltage for the centrifugal pump is calibrated against the centreline velocity of the test section, 750 mm from

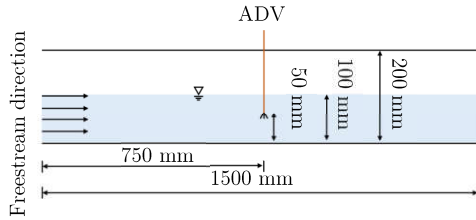


**Figure 4:** Side view of the open flow channel, in schematic form. Also, key dimensions of the experimental setup. The acoustic Doppler velocimeter (ADV) is placed at the same location where the cylinder is located during experimental runs.

the inlet, i.e. mid-length of the test section. We show this schematically in Fig. 4. Here, we define the centreline of the test section as the line 50 mm from the bottom and 50 mm from either of the sidewalls of the test section. We placed the cylinder in the same position during experimental runs.

The centreline velocity  $U_{\text{cent}}$  is measured using an acoustic Doppler velocimeter (ADV), sampling at 200 Hz. The resulting calibration curve is applicable for determining  $U_{\text{cent}}$  at input voltages  $30 < V_{\text{in}}(\text{V}) < 100$ . We measured the turbulence intensity along the centreline to be about 5%.

We obtained the time history for cylinder displacement,  $y$ , by using a video camera pointed normal to the cylinder endplate. We placed a visual marker on the endplate, and the motion of the marker captured by the camera is analysed using *Tracker*: a motion analysis tool built on the Open Source Physics Java framework.

To validate our experimental setup, we tuned to the best of our ability our experimental parameters to the values used by Koide et al. (2013) and test whether we can replicate their results. Table 1 summarises the parameters in lieu of that paper.

**Table 1**

Summary of experimental parameters in contrast to those used in the experimental work of Koide et al. (2013).

	Current study	Koide et al. (2013)
Cylinder diameter, $D$ (m)	0.01	0.01
Cylinder length, $l_{\text{cylinder}}$ (m)	0.09	0.098
Strip-plate width (m)	0.01	0.01
Strip-plate length (m)	0.1	0.1
Effective mass, $m_{\text{eff.}}$ (kg)	0.162	0.174
Logarithmic damping, $\delta$	0.178	0.24
Scruton number, $Sc$	9.94	7.74
System natural frequency, $f_n$ (Hz)	4.42	4.4 to 4.79

We show a sample of the normalised displacement –  $y^* = y/D$  – time series in Fig. 5. Computing the statistics of  $y^*$  and the normalised cylinder vibration frequency,  $f^* = f_{\text{cyl.}}/f_n$  ( $f_{\text{cyl.}}$  being the vibration frequency of the cylinder), from several runs gave us a value of  $y^* = 0.33 \pm 0.03$  and  $f^* = 1.03 \pm 0.04$ . Koide et al. (2013) obtained  $y^* = 0.32$  and  $f^* = 1.09$  under a similar  $U^*$  condition. We thus take this fairly successful reproduction of the results of Koide et al. (2013) as an indication of readiness for further data collection.

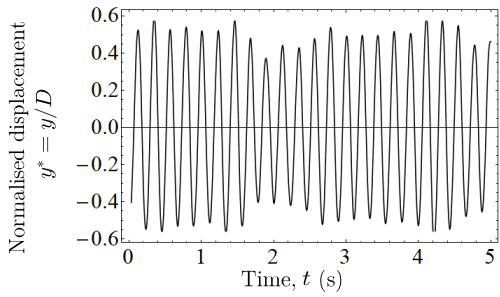


**Figure 5:** A sample of the time history for cylinder displacement from a test run of our experimental setup. the value of  $U^* = 22.7$

### 192 3. Numerical setup validation

#### 193 3.1. Simple grid independency study

194 Numerical solutions of actual, continuous physical phenomena contain errors, or uncertainties, due to temporal  
 195 and spatial discretisation. Reliance on the numerical method of investigation puts the responsibility on the user to  
 196 minimise and justify the magnitude of error introduced in the solution.

197 While CFD users usually point towards their low Courant-Friedrichs-Lowy number to substantiate their claim of  
 198 temporal convergence for their numerical solutions, researchers demonstrate the spatial convergence of their solution  
 199 through either one of these methods. First, by solving the governing equations on several grids, each grid being a  
 200 finer version of the previous one and showing that the quantities of interest are approximately the constant on all grids  
 201 tested. One then chooses the mesh with a medium resolution to use in the subsequent data collection (Wu, 2011; Ding  
 202 et al., 2013, 2015a, 2019).

#### 203 3.2. Grid independency study via Richardson extrapolation and grid convergence index

204 Like the first, the second method solves the governing equations on successively finer grids. However, instead of  
 205 arguing that one obtains similar results on all the grids, the investigator checks whether the quantities of interest tend  
 206 towards value, as one solves the governing equation on successively finer grid resolutions (Richardson and Gaunt, 1927;  
 207 Stern et al., 2001). This method, of checking for convergence pays attention not only on the presumed converged value  
 208 but also on the trend of convergence. Literature that employ this method impose a monotonic convergence condition  
 209 (Stern et al., 2001; Mat Ali et al., 2011; Ali et al., 2012; Maruai et al., 2018) on their quantities of interest, adding an  
 210 extra layer of confidence in the final form of heir spatial discretisation.

211 Additionally, this method allows for a quantitative description of the degree of convergence through the grid conver-  
 212 gence index (GCI). Let  $f_1, f_2, f_3, \dots, f_k$  denote the quantity of interest obtained from several grids. A larger subscript  
 213 indicates a coarser grid, this  $f_1$  denotes the finest while  $f_k$  denotes the coarsest grid. Let the difference between suc-  
 214 cessive solutions be  $\epsilon_{2,1}, \epsilon_{3,2}, \epsilon_{4,3}, \dots, \epsilon_{n,n-1}$ , where  $\epsilon_{2,1} = f_2 - f_1, \epsilon_{3,2} = f_3 - f_2$  and so on. Then, the GCI is defined

215 as

$$\text{GCI}_{i+1,i} = F_s \frac{|\epsilon_{i+1,i}|}{f_i(r^p - 1)} \times 100\%, \quad (15)$$

216 where  $F_s$ ,  $f_i$  and  $r^p$  denotes the safety factor ( $= 1.25$ ), quantity of interest and the refinement ratio,  $r$ , between successive  
 217 grids raised to the order of accuracy of the series of solution,  $p$ . We refer the reader to Stern et al. (2001); Langley  
 218 Research Centre (2018) for a more detailed discussion on  $r^p$ .

219 We can estimate what the solution approaches as the grid size approaches zero by using the  $p^{\text{th}}$  method. Briefly,  
 220 we compute the generalised Richardson extrapolation of the quantity of interest as follows.

$$f_{\text{RE}} = f_1 + \frac{f_1 - f_2}{r^p - 1}, \quad (16)$$

221 where  $f_{\text{RE}}$  is the Richardson extrapolation of the quantity of interest. Using  $f_{\text{RE}}$  to estimate the limit of the monoton-  
 222 ically convergent series of  $f_i$ , we can determine the percentage difference of our solution on our finest grid from this  
 223 limit as

$$E_i = \frac{f_i - f_{\text{RE}}}{f_{\text{RE}}} \times 100\%. \quad (17)$$

224 Table 2 summarises the result of our grid independency study for the SVIV reduced velocity of  $U^* = 22.7$ .  
 225 We identified three quantities central to the investigation of fluid-structure phenomena, especially the flow-induced  
 226 vibration of a circular cylinder. They are the vibration amplitude, vibration frequency and lift coefficient of the cylinder.  
 227 We solve the governing equations on three grids which are numbered 1 for the finest, 2 for the medium and 3 for the  
 228 coarsest, shown in Fig. 6. If we let  $v_i$  be the volume of the  $i^{\text{th}}$  cell in the grid, then, the average cell size is

$$h = \frac{1}{N} \left[ \sum_{i=1}^N v_i \right]^{1/3}, \quad (18)$$

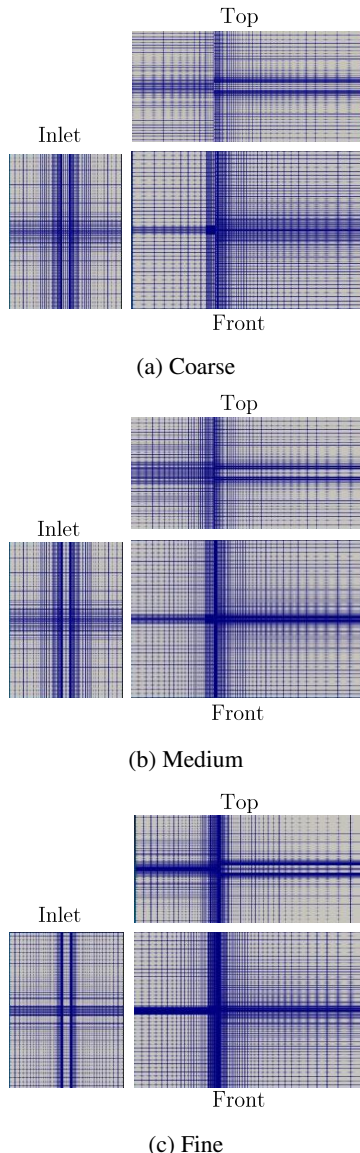


**Figure 6:** Three meshes used in the grid convergence study. Figures 6a, 6b and 6c show the coarse, medium and fine meshes viewed perpendicular to three main viewing positions: from the inlet, the top and the front, which is looking directly at the cylinder end.

229 and the normalised average cell size is hence

$$h/D = \frac{1}{ND} \left[ \sum_{i=1}^N v_i \right]^{1/3}. \quad (19)$$

230 Both  $y_{\text{RMS}}^*$  and  $C_{\text{I RMS}}$  starts at an initial value smaller than their Richardson extrapolations,  $f_{\text{RE}}$ , before approaching  
231 it as we decrease the average cell size,  $h$ . This similar trend can perhaps be attributed to the causal relationship between

the lift coefficient and vibration amplitude. The lift drives and sustains the vibration, hence a small lift produces a small vibration, and when the lift amplitude becomes higher, so too does the vibration amplitude. The vibration frequency, on the other hand, starts at a value larger than its  $f_{RE}$  before approaching  $f_{RE}$ .

The quantity  $Cl_{RMS}$  experiences the most significant drop in GCI as we refine the grid. The GCI is close to one-third (30.92%) as we refine the grid from coarse to medium with a refinement ratio of 1.376. The refinement ratio is calculated by dividing the number of cells in one grid with the next one down the refinement line. Following the grid numbering convention explained previously, dividing the number of cells in the fine grid (grid 1) with the number of cells in the medium grid (grid 2) gives us the refinement ratio from medium to fine, or  $r_{2,1}$ . Similarly, dividing the number of cells in the medium grid (grid 2) with the number of cells in the coarse grid (grid 3) gives us the refinement ratio from coarse to medium, or  $r_{3,2}$ . We can generalise this to  $i$ -number of grids as follows.

$$r_{i+1,i} = \frac{S_{\text{grid},i+1}}{S_{\text{grid},i}}, \quad (20)$$

where  $S_{\text{grid},i}$  denotes the total number of cells in the  $i^{\text{th}}$  grid. The GCI of  $Cl_{RMS}$  drops further to 1.63% as the mesh is refined more with a refinement ratio of 1.304.

The GCI for  $y_{RMS}^*$  also drops by one order of magnitude as can be seen by comparing  $GCI_{3,2}$  with  $GCI_{2,1}$ . Again, this similar trend of improvement points to the causal relationship between lift and displacement of the cylinder. The GCI for  $f^*$ , however, drops by approximately a factor of 6 instead of one order of magnitude, unlike the GCIs of  $y_{RMS}^*$  and  $Cl_{RMS}$ .

**Table 2**  
Summary of grid independency study.

Parameter/ metric	$Cl_{RMS}$	$y_{RMS}^* = y^*/D$	$f^* = f_{cyl.}/f_n$
$f_{RE}$	0.262	0.369	0.969
$f_1$	0.2598	0.3687	0.9695
$f_2$	0.2430	0.3588	0.9740
$f_3$	0.0805	0.2374	1.0220
$ \epsilon_{2,1} $	0.02	0.01	0.004
$ \epsilon_{2,1} $	0.16	0.12	0.48
$R =  \epsilon_{2,1}  /  \epsilon_{1,1} $	0.10	0.08	0.094
$GCI_{3,2}$	30.92	6.00	0.64
$GCI_{3,2}$	1.63	0.52	0.10

We provide visual representations of the convergent  $Cl_{RMS}$ ,  $y_{RMS}^*$  and  $f^*$  series in Figs. 7, 8 and 9. Note how the quantity of interest is very close to its Richardson extrapolation at the fine grid (grid 1) for all  $Cl_{RMS}$ ,  $y_{RMS}^*$  and  $f^*$ . This implies that the fine grid already provides adequate spatial discretisation for the problem we are studying, and further refinements, while able to nudge our solutions even closer to the limit that is the Richardson extrapolation, may

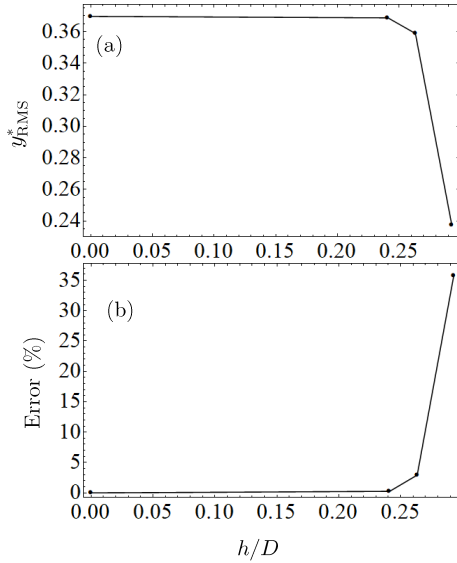


**Figure 7:** The convergence diagram for  $y^*_{\text{RMS}}$ . Figure 7a shows how  $y^*_{\text{RMS}}$  converges close to the Richardson extrapolation value while Fig. 7b shows how the error (difference between the value obtained from a particular mesh and the Richardson extrapolation) decreases with decreasing grid spacing.

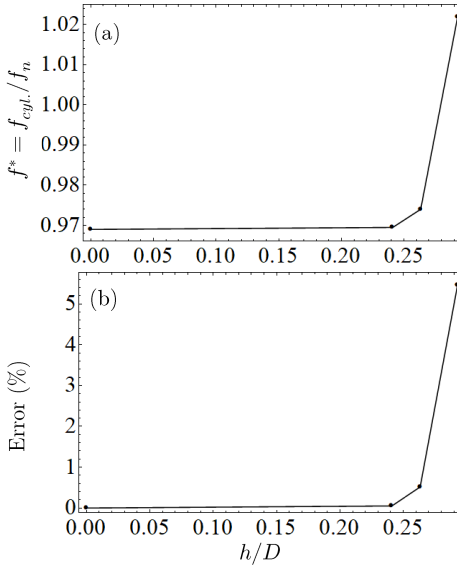


**Figure 8:** The convergence diagram for  $f^*$ . Figure 8a shows how  $f^*$  converges close to the Richardson extrapolation value while Fig. 8b shows how the error (difference between the value obtained from a particular mesh and the Richardson extrapolation) decreases with decreasing grid spacing.

not be optimal in terms of usage of computational resources. Values of  $y^*_{\text{RMS}}$  and  $f^*$  at the fine grid already fall within experimental uncertainty as evidenced by our measurement in §2.4 and the work by Koide et al. (2013). Hence, all succeeding numerical data are gathered from the fine grid.

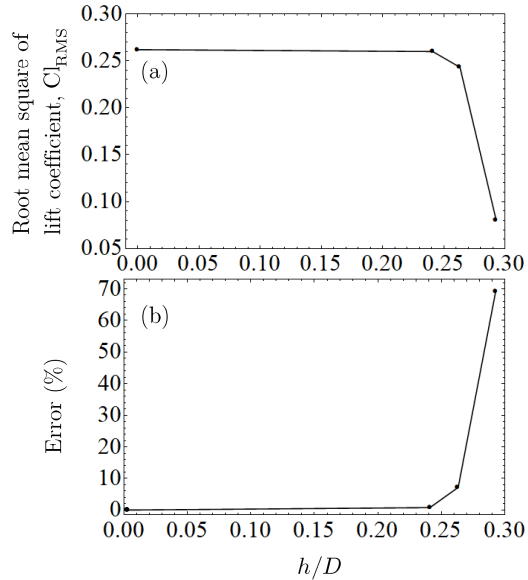


**Figure 9:** The convergence diagram for  $Cl_{RMS}$ . Figure 9a shows how  $Cl_{RMS}$  converges close to the Richardson extrapolation value while Fig. 9b shows how the error (difference between the value obtained from a particular mesh and the Richardson extrapolation) decreases with decreasing grid spacing.

## 255 4. Single plate amplitude and frequency response

### 256 4.1. Amplitude response

257 We compared our experiment and numerical results with those from Koide et al. (2013) and Nguyen et al. (2012) in  
 258 Fig. 10. Figure 10a shows the amplitude response of our single plate experiment and simulation. We use the root-mean-  
 259 square value of the cylinder displacement to represent the amplitude responses instead of the maximum displacement.  
 260 The reason for this is twofold: first, using  $y_{RMS}^*$  facilitates comparison of data with Nguyen et al. (2012) and Koide  
 261 et al. (2013), who also used  $y_{RMS}^*$  in their work. Second, because the cylinder displacement is an intermediate quantity  
 262 for the estimation harnessed power (Maruai et al., 2017, 2018), the usage of root-mean-square of cylinder displacement  
 263 gives a preview of mean harnessed power, once the vibration is converted into alternating current.

264 There is virtually no vibration for both our experiment and simulation when  $U^* < 18$ , except for a small peak close  
 265 to 0.1 at  $U^* \approx 7$ . We attribute this peak to the upper branch of KVIV, which still exists, although suppressed due to  
 266 the cruciform configuration of the system (Shirakashi et al., 1989; Nguyen et al., 2012). However, when  $U^*$  exceeds  
 267 18, we observe a sudden jump in  $U^*$  right up to about 0.4, for both our experiment and simulation. This we attribute  
 268 to the formation of the streamwise vortices that drive SVIV.

269 After the inception of SVIV, the value for  $y_{RMS}^*$  drops down to approximately 0.3, before recovering to a value  
 270 that is close to what was observed by Nguyen et al. (2012) and Koide et al. (2013). This sudden jump followed by a  
 271 gradual drop and a gradual rise in  $y_{RMS}^*$  was not found in the works of Nguyen et al. (2012) nor Koide et al. (2013),

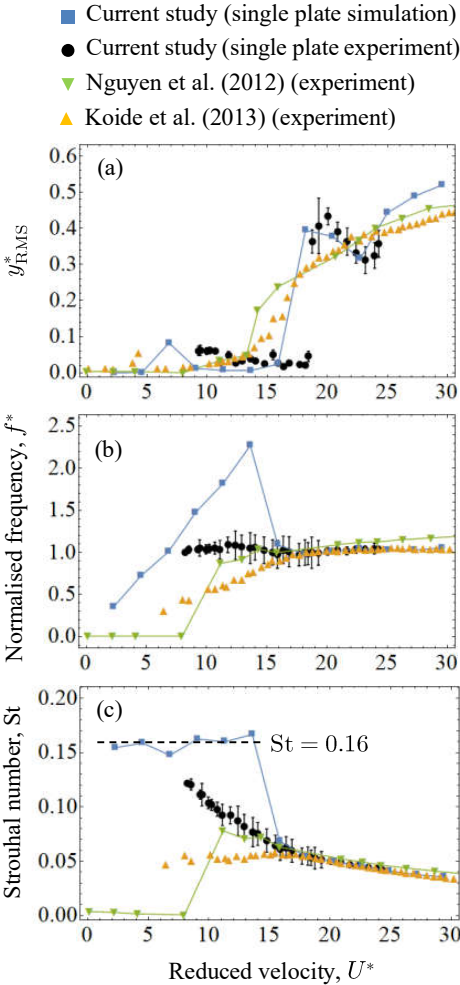


**Figure 10:** The amplitude and frequency response of our cruciform system, compared with results from Nguyen et al. (2012) and Koide et al. (2013). Figure 10a shows the amplitude response using  $y^*_{\text{RMS}}$ , Fig. 10b the frequency response using  $f^*$  and Fig. 10c also the frequency response, but using the Strouhal number of vibration.

even though their experimental parameters are reasonably close to what we use in both our experiment and simulation.

We, therefore, attribute this difference to the higher turbulence level set in our work. The turbulence level in the works of Nguyen et al. (2012), for example, was  $< 2.8\%$  throughout their range of Reynolds number. Instead, the initial turbulence level in our setup, both experimental and numerical, is approximately double that value. Because of this, the turbulence amplification due to the onset of streamwise vortices (Zhao and Lu, 2018) — especially for a circular cylinder-strip plate cruciform (Koide et al., 2017) — is also higher compared to the experiments of Nguyen et al. (2012) and Koide et al. (2013). This higher compound turbulence warps the dominant vortical structure and introduces an increasing amount of intermittency to the lift signal, and by extension, to the displacement time history of the cylinder.

One can simply inspect the error bars within  $18 < U^* < 23$  in Fig. 10a to verify the greater sample dispersion

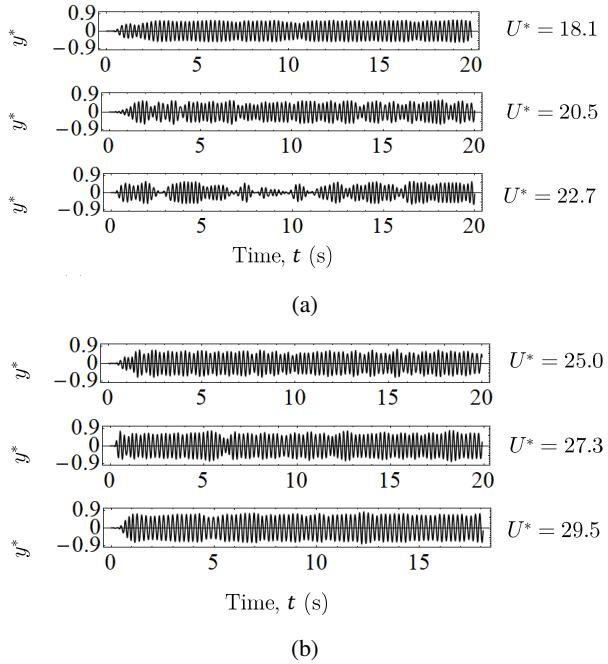


**Figure 11:** The time series of cylinder displacement between  $18 < U^* < 20$ . Fig. 11a groups the cylinder displacement signal between  $18 < U^* < 23$ , where there seems to be an increase in intermittency in the displacement signal, while Fig. 11b groups the cylinder displacement signal between  $25 \leq U^* < 30$ , where the intermittency in the displacement signal vanishes.

282 within that range of  $U^*$ . This intermittency ultimately vanishes as the dominant vortical structures become sufficiently  
 283 stable to retain enough periodicity in its formation. Our numerical results also seem to support this argument, as  
 284 evidenced by the time history of  $U^*$  within  $18 < U^* < 30$  in Fig. 11. There exists a distinct increase in intermittency  
 285 for the time histories in Fig. 11a, that disappears once  $U^* > 23$  as can be seen in Fig. 11b.

## 286 4.2. Frequency response

287 Figure 10b compares the frequency responses of our experiment and numerical results with those in Nguyen et al.  
 288 (2012) and Koide et al. (2013). We use the normalised frequency  $f^*$  in Fig. 10b and the vibration Strouhal number in  
 289 Fig. 10c to aid comparison between the results. In our experiments, the value for  $f^*$  always fall close to unity. However,  
 290 if we inspect the size of the error bars, we observed a range of  $U^*$  where there exists a higher degree of variance in  
 291 the sample measurements between  $13.6 \leq U^* \leq 20.5$ . The reason for this lies in  $13.6 \leq U^* \leq 20.5$  coinciding with  
 292 the desynchronization region of the KVIV regime up to  $U^* = 18.2$ , and then overlaps with the intermittent vibration  
 293 of SVIV up to  $U^* = 20.5$ . Within these two regimes, the cylinder displacement time history – from which  $f^*$  is  
 294 calculated – varies considerably in amplitude and periodicity, resulting in larger error bars. In Fig. 10c we can see the  
 295 overall trend being more similar to the results of Koide et al. (2013) rather than Nguyen et al. (2012), which is likely  
 296 due to a higher similarity between our experimental setup with that of Koide et al. (2013), most striking in terms of

297 the gap ratio  $G = g/D$ , which is identical.

298 Our numerical results exhibit a significantly different trend, but only up to  $U^* = 15.9$ . We observe in Fig. 10b that  
299 the vibration frequency of the cylinder increases linearly, even past  $U^* = 6.8$ , which is the upper branch of the KVIV  
300 regime. Converting  $f^*$  into Strouhal number reveals that the cylinder is vibrating close to the Karman frequency of  
301 the system. The Karman frequency of a smooth, fixed circular cylinder refers to the shedding frequency of Karman  
302 vortices in its wake. An empirical relationship with Reynolds number exists for  $250 < \text{Re} < 2 \times 10^5$ , which is the  
303 following Blevins (1990).

$$\text{St} = 0.198 \left( 1 - \frac{19.7}{\text{Re}} \right) \quad (21)$$

304 The values we get using Eq. 21 are nearly constant about 0.19 for  $U^* \leq 13.6$ . The slight discrepancy from our  
305 Strouhal number mean ( $\approx 0.16$ ) in the  $U^* \leq 13.6$  range can be ascribed to us studying a cruciform structure instead  
306 of the smooth circular cylinder upon which Eq. 21 was originally based (Blevins, 1990).

307 The discrepancies found especially in Fig. 10b most probably stem from the same reasons explained by Nguyen  
308 et al. (2012). The lowest  $y_{\text{RMS}}^*$  recorded in our simulation within  $6.8 \leq U^* \leq 13.6$  was in the order of  $10^{-5}$  m (10  
309 microns). A numerical study has no problem recording vibration of this order as the precision of the numerical solution  
310 is only limited by the processor architecture. Experimental work, however, requires not only the sensitivity but also  
311 the isolation from the background noise that forces the cylinder to vibrate close to the natural frequency of the system  
312  $f_n$  (Nguyen et al., 2012), which consequently overpowers this minimal amplitude vibration. Once streamwise vortices  
313 form, however, their shedding and cylinder vibration synchronises close to  $f_n$ , thus locking the normalised vibration  
314 frequency back to  $f^* \approx 1$ .

## 315 5. Temporal evolution of the lift coefficient

### 316 5.1. Ensemble empirical mode decomposition and Hilbert transform

317 To obtain a clearer picture of the temporal characteristics of the lift and cylinder displacement signals, we decided  
318 to employ the ensemble empirical mode decomposition (EEMD) method (Huang et al., 1998; Wu and Huang, 2008)  
319 on the signals, and compute their instantaneous phase lag, frequency and amplitude using the Hilbert transform.

320 The Hilbert transform (HT) has been used in the past to study the instantaneous phase and frequencies of KVIV  
321 (Khalak and Williamson, 1999). However, the signal must be monochromatic if we are to obtain a physically mean-  
322 ingful result after applying HT. EEMD is a way to pre-process the signal and get components that (1) have zero mean,  
323 and (2) have an equal number of extrema and zero crossings, or they differ only by one. Functions that fulfil these

324 criteria are called intrinsic mode functions (IMF), and they guarantee a physically meaningful result to HT (Gumelar  
325 et al., 2019; Zhou et al., 2019). Unlike Fourier transform, which is an analytical method of signal decomposition based  
326 on circular functions in the complex plane, EEMD is algorithmic, and the processes undertaken can be summarised as  
327 follows.

328 Produce 150 white noise signals of length equal to the original signal and amplitude equal to 0.2 of the standard  
329 deviation of the original signal. Then, add to the set of white noises the original signal – creating 150 variations of  
330 the original signal. Following that, we apply the empirical mode decomposition (EMD) algorithm on each of the 150  
331 signals. The EMD algorithm is summarised below.

- 332 1. Construct the envelope of the signal by connecting all maxima/minima with cubic splines.
- 333 2. Find the local mean of the envelope for the span of the data.
- 334 3. Find the difference between the local mean and the original data.
- 335 4. Repeat steps 1 and 2 on the difference in 3 for ten times (Wu and Huang, 2008).

336 The steps above produce a set of intrinsic mode functions or IMFs for each of the 150 variations of the original  
337 signal. Then, we average the first IMF component from each of the decomposed original signal variations, to obtain  
338 the first EEMD IMF  $C_1$  of the original signal. We do the same for the second, third, until the  $n^{\text{th}}$  component for each  
339 of the 150 original signal variations, thus obtaining  $C_2, C_3, \dots, C_n$ .

340 To compute the phase lag between the characteristic IMFs of the lift coefficient and normalised cylinder displace-  
341 ment, we select the IMF components with the highest correlation to the  $y^*$  signal at that particular  $U^*$ , to represent the  
342 signals, denoted as  $C_{y^*, y^*}$  for the characteristic normalised cylinder displacement, and  $C_{Cl, y^*}$  as the characteristic lift  
343 coefficient signal. The phase lag, instantaneous frequency and instantaneous amplitude of the signal is subsequently  
344 computed by taking the constructing an analytical signal  $z(t)$  from  $C_1, C_2, \dots, C_n$  by computing the Hilbert transform  
345 of the IMF,  $H_i$ ,

$$H_i(t) = \frac{1}{\pi} \text{PV} \int \frac{C_i(\tau)}{t - \tau} d\tau, \quad (22)$$

where PV denotes the Cauchy principal value, and then constructing the analytical signal as follows.

$$z(t) = C_i(t) + iH_i(t) \quad (23)$$

346 Note that  $i$  in Eq. 23 is the complex number.

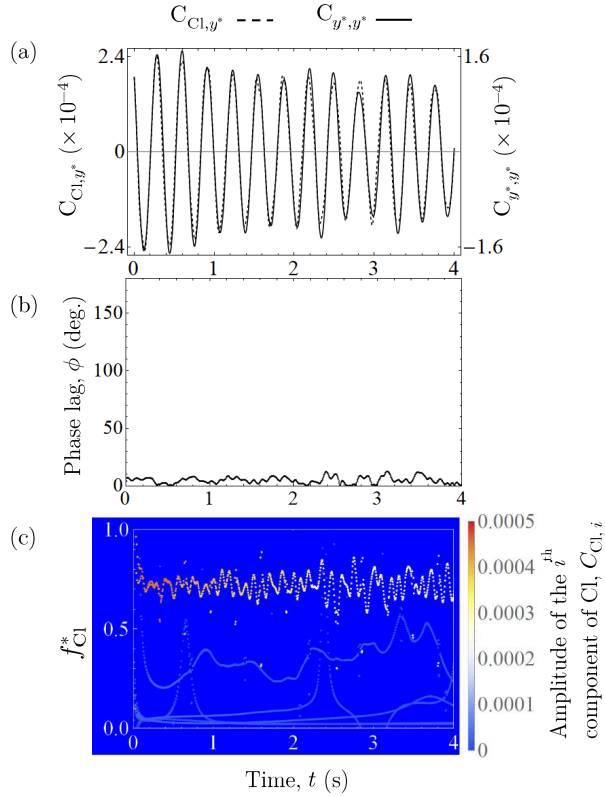


**Figure 12:** Temporal analysis of the lift coefficient and normalised cylinder displacement signal at  $U^* = 4.5$ . We show  $C_{Cl,y^*}$  and  $C_{y^*,y^*}$  side by side in Fig. 12a, present the temporal evolution of the phase lag  $\phi$  in Fig. 12b and show the temporal evolution of the instantaneous frequency of the lift coefficient signal in Fig. 12c.

We refer the reader interested in the details of EEMD and Hilbert transform, also collectively known as the Hilbert-Huang transform (HHT), to the following excellent texts on the subject (Huang and Attoh-Okine, 2005; Huang, 2014).

## 5.2. The KVIV regime ( $U^* \leq 13.6$ )

At reduced velocities  $U^* = 2.3$  and  $4.5$ , the phase lags  $\phi$  (deg.) between Cl and  $U^*$  are practically zero throughout the whole observation time. The characteristic IMFs of Cl and  $y^*$  at  $U^* = 4.5$  exemplifies this trend, as showcased in Fig. 12. Here, Fig. 12a shows the temporal evolution of  $C_{y^*,y^*}$  and  $C_{Cl,y^*}$ , which are the characteristic IMFs of  $y^*$  and Cl, respectively. Figure 12b shows the phase lag between  $C_{y^*,y^*}$  and  $C_{Cl,y^*}$ , and Fig. 12c presents the HHT spectrogram of Cl. The HHT spectrogram visualises the instantaneous frequency and amplitude of the IMF components of Cl. The trend that one notices in Fig. 12b is similar to what was observed in Khalak and Williamson (1999), a study that also employs the Hilbert transform to obtain the instantaneous phase, albeit without EEMD. The dominant IMF component (IMF component sustaining the highest amplitude throughout the whole observation time) of the lift coefficient has a normalized frequency  $f_{Cl}^* = f_{Cl}/f_n$  (Fig. 12c) centred at approximately  $f_{Cl}^* = 0.75$ .

Once we enter the upper branch of KVIV at  $U^* = 6.8$ ,  $\phi$  jumps to approximately 110 deg. This jump in  $\phi$  is

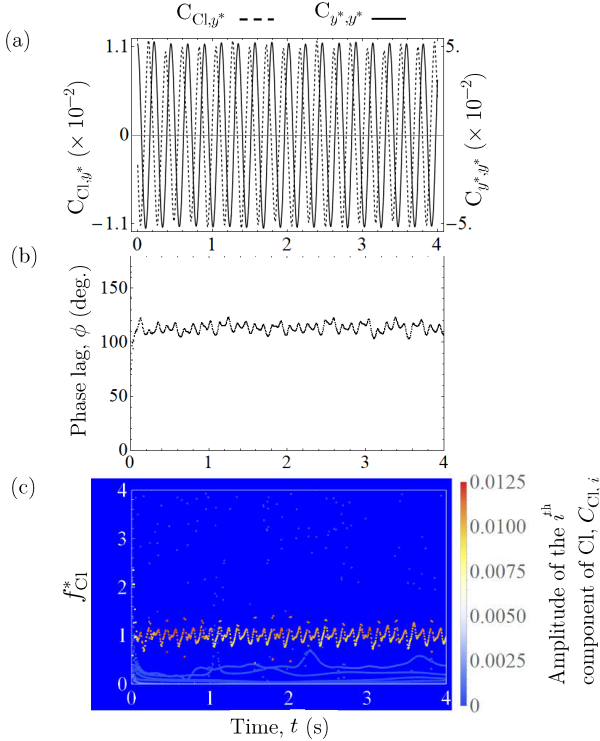


**Figure 13:** Temporal analysis of the lift coefficient and normalised cylinder displacement signal at  $U^* = 6.8$ . We show  $C_{Cl,y^*}$  and  $C_{y^*,y^*}$  side by side in Fig. 13a, present the temporal evolution of the phase lag  $\phi$  in Fig. 13b and show the temporal evolution of the instantaneous frequency of the lift coefficient signal in Fig. 13c.

characteristic of the transition to the upper branches as also observed by Maruai et al. (2018), among others. Both  $C_{Cl,y^*}$  and  $C_{y^*,y^*}$  signals are visibly very periodic, and the dominant frequency band of Cl, is centred at  $\approx 1$ , as one can verify in Fig. 13c.

As we increase  $U^*$  even further up to  $U^* = 13.6$ , we see a similar trend for all  $U^* = 9.1, 11.4, 13.6$  examined:  $C_{y^*,y^*}$  and  $C_{Cl,y^*}$  are both qualitatively very periodic. Their phase lags are very close to 180 deg., and the dominant Cl frequency bands exhibit a mean that increases linearly with respect to  $U^*$ , in a manner that the Strouhal number of Cl is always  $\approx 0.16$  on average. We present the representative case of  $U^* = 13.6$  in Fig. 14. Note how  $\phi$  in this range of  $U^*$  varies much less with respect to time, compared to  $\phi$  at  $U^* = 6.8$ , and the dominant frequency band of Cl is much narrower compared to the dominant frequency band at  $U^* = 6.8$ , indicating a highly periodic and self-similar oscillation of lift.

### 5.3. Transition to SVIV ( $15.9 \leq U^* \leq 18.2$ )

Previously in the  $U^* \leq 13.6$  range, we observed that the temporal profile of both Cl and  $y^*$  are very similar to each other, except that Cl leads  $y^*$  by a certain amount. This similarity in profile supports the assertion that the vibration within  $U^* \leq 13.6$  is driven exclusively by the shedding of Karman vortices, which brings the onset of the alternating

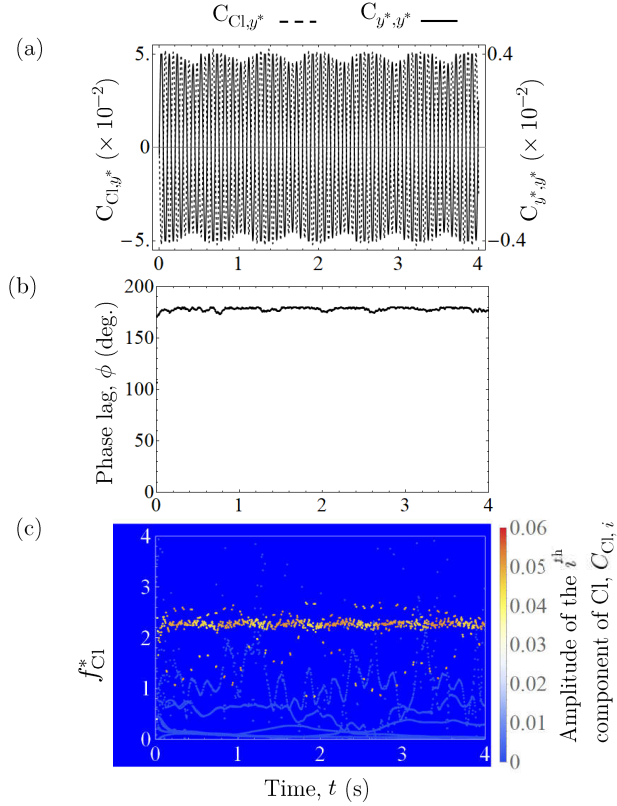


**Figure 14:** Temporal analysis of the lift coefficient and normalised cylinder displacement signal at  $U^* = 13.6$ . We show  $C_{Cl,y^*}$  and  $C_{y^*,y^*}$  side by side in Fig. 14a, present the temporal evolution of the phase lag  $\phi$  in Fig. 14b and show the temporal evolution of the instantaneous frequency of the lift coefficient signal in Fig. 14c.

374 lift. Analogously, one might expect a similar profile between Cl and  $y^*$  when streamwise vortices drive the vibration.  
 375 However, this does not seem to be the case.

376 Once we reach  $U^* = 15.9$ , we observe that it has become difficult to argue that the profile of  $y^*$  is just a lagged  
 377 version of the profile of Cl. This is shown in Fig. 15a, with the enlarged version in Fig. 15b. The profile of Cl looks  
 378 like the result of several signals in superposition, which one can almost distinguish from the presence of two types of  
 379 maxima at two different amplitude heights. We put a red dashed line and a red dashed-dot line in Fig. 15b as visual cues  
 380 indicating the two amplitude heights. Decomposing the lift coefficient signal using EEMD reveals partial evidence  
 381 supporting the compound signal hypothesis.

382 Once we have decomposed the signal using EEMD, we replot Fig. 15a using  $C_{Cl,y^*}$  and  $C_{y^*,y^*}$  in Fig. 16a. One  
 383 can clearly see that the part of Cl signal responsible for driving the vibration at  $U^* = 15.9$  is embedded in the original  
 384 Cl signal, and decomposition via EEMD managed to recover this signal, which leads  $C_{y^*,y^*}$  by approximately 150  
 385 deg. on average, throughout the whole observation time (Fig. 16b). This decline from  $\phi \approx 180$  deg. at reduced  
 386 velocities  $9.1 \leq U^* \leq 13.6$ , to  $\phi \approx 150$  deg. at  $U^* = 15.9$  is quite sizeable, suggesting a fundamental change in flow

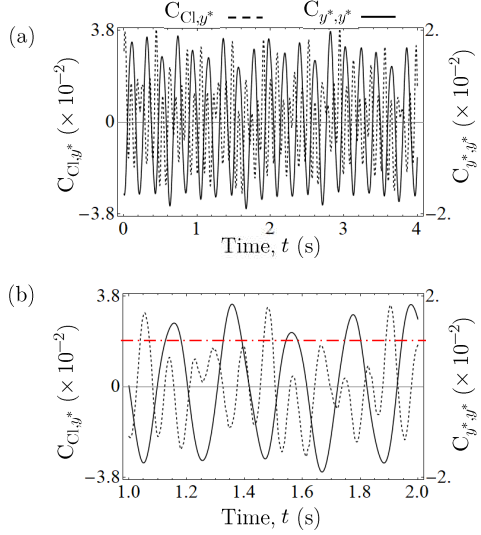


**Figure 15:** Temporal evolution of  $y^*$  and Cl at  $U^*15.9$ . Figure 15b shows an enlarged view of Fig. 15a. We can barely spot semblance of two signals with different amplitudes superimposed in the Cl signal in Fig. 15b.

387 dynamics, particularly in terms of vortical structure. Another notable change is the increased temporal variation in  $\phi$   
 388 from its time-averaged value, in contrast to the evolution of  $\phi$  in the range  $9.1 \leq U^* \leq 13.6$ , which has very little jitter  
 389 throughout the observation time.

390 Inspecting the HHT spectrogram in Fig. 16c reveals two dominant bands in the frequency domain. The first one,  
 391 marked with a white continuous rectangular box, is the instantaneous frequency for the IMF component of lift shown  
 392 in Fig. 16a, and its mean frequency lies close to the natural frequency of the system ( $f_{Cl}^* \approx 1$ ). There is; however, a  
 393 second band of the frequency with nearly similar amplitude around  $f_{Cl}^* \approx 3.3$ , marked with a white dashed rectangular  
 394 box. Computing the Strouhal number from this frequency returns a value of  $St = 0.20$ , which is very close to the  
 395 Strouhal number for Karman vortices as predicted by Eq. 21 at the Reynolds number equivalent to  $U^* = 15.9$ , which  
 396 is  $Re = 7.9 \times 10^3$ . We thus attribute this second band of frequency as being the footprint left by the shedding of  
 397 Karman vortices, and the first band as the result of streamwise vortex shedding. Through visual inspection of Fig. 16c,  
 398 both of these dominant frequency bands are markedly wider and the individual values are more scattered from their  
 399 time-averaged values than any of their counterparts within  $U^* \leq 13.6$ .

400 The knowledge that Karman vortices continue to exist and shed from a cruciform structure during SVIV is not  
 401 new in the literature. However, this is the first time the lift signal from a cruciform structure undergoing SVIV has  
 402 been subjected to EEMD, revealing the signature of the two dominant vortical structures regulating the flow around  
 403 the cruciform. Although the amplitude size of the instantaneous frequency band due to Karman vortex is comparable  
 404 to the streamwise vortex, the reason why the cylinder resists locking into its frequency is perhaps that its frequency too  
 405 distant from the natural frequency of the system  $f_n$ . The shedding frequency of the streamwise vortex is much closer

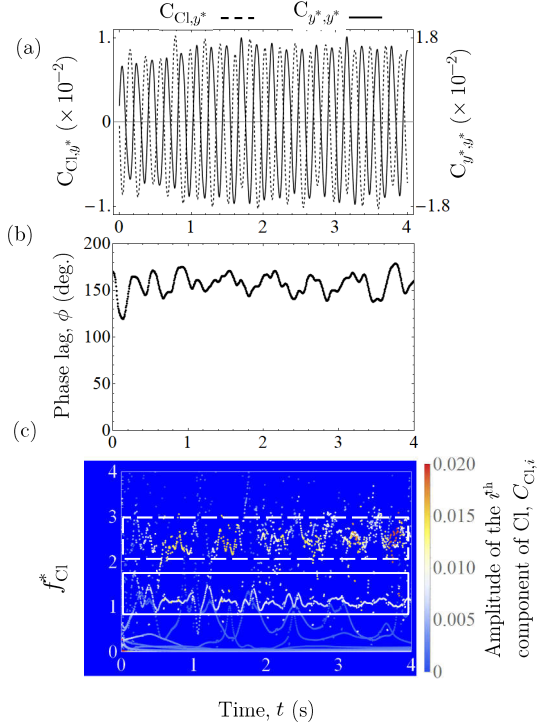


**Figure 16:** Temporal analysis of the lift coefficient and normalised cylinder displacement signal at  $U^* = 15.9$ . We show  $C_{Cl,y^*}$  and  $C_{y^*,y^*}$  side by side in Fig. 16a, present the temporal evolution of the phase lag  $\phi$  in Fig. 16b and show the temporal evolution of the instantaneous frequency of Cl in Fig. 16c.

406 to  $f_n$  and is thus preferred by the cylinder.

407 We consider the transition to SVIV to be complete at  $U^* = 18.2$ , when the time-averaged phase lag drops further to  
 408  $\approx 20$  deg. Figure 17a and 17b documents this observation. The instantaneous phase lag is observed to slip through 360  
 409 deg. a little past the two second (2 s) timestamp. By inspecting Fig. 17a, we found that a little past 2 s is when distortions  
 410 in the periodicity of  $C_{Cl,y^*}$  occur. The slipping through 360 deg. was also observed by Khalak and Williamson (1999)  
 411 in their work on KVIV, highlighting the quasi-periodic nature of the signal being analysed. There, the slip appeared  
 412 in Khalak and Williamson (1999) at the initial branch of KVIV. The overall low value of  $\phi$  ( $\approx 20$  deg. for the whole  
 413 observation time at  $U^* = 18.2$ ), coupled with the presence of  $\phi$  slippage are suggestive of the possibility for  $U^* = 18.2$   
 414 being the initial branch of SVIV.

#### 415 5.4. The stable SVIV regime ( $U^* \geq 20.5$ )

416 As  $U^*$  is increased to 20.5, we can see a jump in  $\phi$  from a mean value of approximately 20 deg. to about 120 deg.,  
 417 shown in Fig. 18a. The phase slippage discussed previously is also observed, indicating the quasi-periodic nature  
 418 of the lift coefficient signal at this  $U^*$ . Incidentally, this quasi-periodicity seems to be the norm for the lift signals  
 419 up to  $U^* = 27.3$ , as suggested by the phase slippages evident in Figs. 17b, c and d. The slippage only stops once

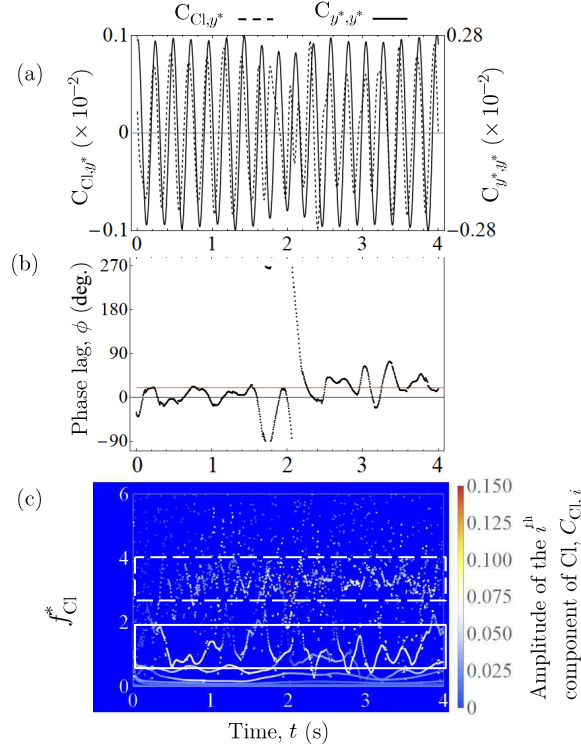


**Figure 17:** Temporal analysis of the lift coefficient and normalised cylinder displacement signal at  $U^* = 18.2$ . We show  $C_{Cl,y^*}$  and  $C_{y^*,y^*}$  side by side in Fig. 17a, present the temporal evolution of the phase lag  $\phi$  in Fig. 17b and show the temporal evolution of the instantaneous frequency of  $Cl$  in Fig. 17c.

420  $U^*$  reaches 29.5, suggesting a more periodic behaviour of the lift coefficient compared to its counterparts between  
 421  $20.5 \leq U^* \leq 27.3$ . Although the instantaneous phase between  $20.5 \leq U^* \leq 27.3$  implies a quasi-periodic nature,  
 422 their mean values at each  $U^*$  are contained in the narrow region  $114 < \phi$  (deg.)  $< 135$ , as is the value for  $\phi$  at  
 423  $U^* = 29.5$ . This observation that the value of  $\phi$  is only slowly varying with respect to  $U^*$ , once  $U^*$  increases past  
 424 20.5, can be interpreted as the dominant flow structures settling into a stable form that becomes more resilient against  
 425 external excitations. Based on this feature, we classified  $20.5 \leq U^* \leq 29.5$  as the upper branch of SVIV.

426 The data on the evolution of  $\phi$  allows us to construct a map of the “branches” of vibration modes observed in the  
 427 range of  $U^*$  that we studied. As the branches are mapped against  $U^*$ , we need a representative value of  $\phi$  at each  
 428  $U^*$ . To achieve this, we took the time-averaged values of  $\phi$ , i.e.  $\phi_{\text{mean}}$ , and plotted them against  $U^*$  in Fig. 19. The  
 429 region A indicates the initial branch of KVIV, where  $\phi_{\text{mean}}$  is close to zero. Region B denotes the upper/lower branch  
 430 of KVIV, where the system experiences a jump from  $\phi_{\text{mean}} \approx 0$  to greater than 110 deg. The value of  $\phi_{\text{mean}}$  settles  
 431 very close to 180 deg. towards the end of this upper/lower branch.

432 Then,  $\phi_{\text{mean}}$  experiences a slight drop from about one-sixth the value of  $\phi_{\text{mean}}$  in region B, as we enter region C,  
 433 marking the start of the transition to the SVIV regime. Following this, the system undergoes a more sudden drop to

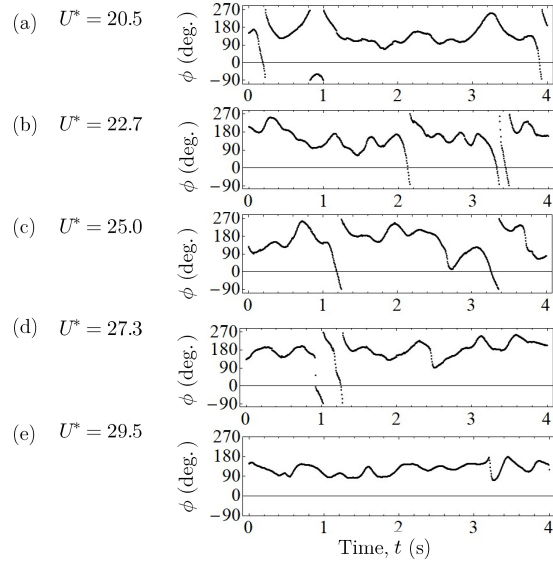


**Figure 18:** The instantaneous phase lag  $\phi$  of  $C_{Cl,y^*}$  in the range  $20.5 \leq U^* \leq 29.5$ . We can observe  $\phi$  slipping through 360 deg. between  $20.5 \leq U^* \leq 27.3$ , before disappearing at  $U^* = 29.5$ ; an indication of improved stability and resilience of the vortical structure driving the vibration.

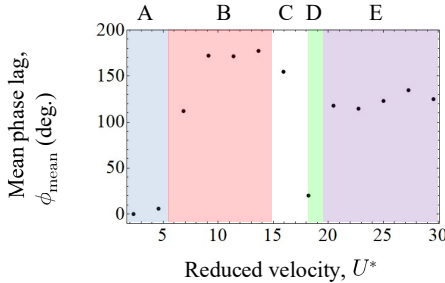


**Figure 19:** Vibration regimes identified during analysis of  $\phi$ . To capture the evolution of  $\phi$  with respect to  $U^*$ , a representative value for  $\phi$  at each  $U^*$  must be selected. We chose to use the time-averaged  $\phi$ ,  $\phi_{mean}$ , as the representative value.

434  $\phi_{mean} \approx 20$  deg. at  $U^* = 18.2$ . This we designate as region D. Finally, in region E, we observe another jump in  $\phi_{mean}$   
 435 from  $\phi_{mean} \approx 20$  deg. in region D to approximately 120 deg. when  $U^* \geq 20.5$ .

## 436 6. Estimation of harnessable power

### 437 6.1. Mathematical model for power estimation

438 The mathematical model for harnessable power estimation in this study follows that which had been derived in  
 439 Raghavan et al. (2007). In these works, the authors mentioned that work done by the oscillating cylinder  $W_{cyl}$  during

440 one cycle of oscillation  $T_{\text{osc.}}$  is as follows.

$$W_{\text{cyl.}} = \int_0^{T_{\text{osc.}}} (F_L \cdot \dot{y}) dt \quad (24)$$

441 where both the lift  $F_L$  and cylinder velocity  $\dot{y}$  are both functions of time. Through several manipulations and simplifying  
 442 assumptions (Sun et al., 2016), the power captured by the system can be written, using our parameters, as the fluid  
 443 power

$$P_{\text{Fluid,RMS}} = \frac{1}{2} \rho \pi C_{\text{Cl,RMS}} U^2 f_{\text{cyl.}} y_{\text{RMS}}^* D L \sin(\phi), \quad (25)$$

444 or the mechanical power

$$P_{\text{Mech.,RMS}} = 8\pi^3 m_{\text{eff.}} \zeta_{\text{tot.}} (y_{\text{RMS}}^* f_{\text{cyl.}})^2 f_n. \quad (26)$$

445 Here,  $P_{\text{Fluid,RMS}}$ ,  $P_{\text{Mech.,RMS}}$ ,  $L$ ,  $C_{\text{Cl,RMS}}$ ,  $\zeta_{\text{tot.}}$  and  $m_{\text{eff.}}$  are the root-mean-square of fluid power, root-mean-square  
 446 of mechanical power, length of the circular cylinder, characteristic root-mean-square of lift amplitude, total damping  
 447 coefficient, and the system effective mass respectively. We compute  $C_{\text{Cl,RMS}}$  in Eq. 25 by taking the root-mean-square  
 448 amplitude of  $C_{\text{Cl},y^*}$ . We choose to use root-mean-square (parameters with subscript RMS) quantities in Eq. 24 instead  
 449 of the maximum values like the original authors because that may lead to a misunderstanding that the maximum value  
 450 is sustained throughout the observation window. This obviously is not always the case in our study, especially once  
 451 the system transits into the SVIV regime. Recall that the time series analysis of  $y^*(t)$  and  $\text{Cl}(t)$  in §4.1 revealed  
 452 that there is a degree of intermittency in both signals that cannot be overlooked at certain ranges of  $U^*$ . Using the  
 453 root-mean-square value allows us to partially take this into account in the estimation of harnessable power.

454 Figure 20 shows the comparison between power estimated from our experiment and numerical results, with the  
 455 experimental results of Nguyen et al. (2012) and the direct power measurement of Koide et al. (2013). Only the value  
 456 for  $P_{\text{Mech.,RMS}}$  is computed from our experimental results due to the absence of lift data. Our numerical results have  
 457 both lift and cylinder displacement data, and hence, we calculated both  $P_{\text{Fluid,RMS}}$  and  $P_{\text{Mech.,RMS}}$ . We estimated the  
 458 power from the experimental results of Nguyen et al. (2012) by interpolating missing data points in both their amplitude  
 459 and frequency responses to compute the value of  $P_{\text{Mech.,RMS}}$  at a given value of  $U^*$ . The direct power measurement  
 460 by Koide et al. (2013) was done by connecting the elastic support of the cylinder to a coil. The coil moves with the

- $P_{\text{Mech.,RMS}}$ , current study (experiment)
- $P_{\text{Fluid,RMS}}$ , current study (numerical)
- $P_{\text{Mech.,RMS}}$ , current study (numerical)
- ▶  $P_{\text{Measured,RMS}}$ , Koide et al. (2013) (experiment)
- △  $P_{\text{Mech.,RMS}}$ , Nguyen et al. (2012) (experiment)

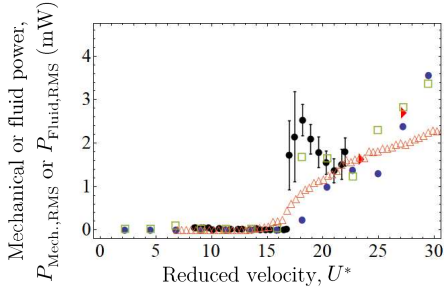


**Figure 20:** Estimated root mean square of mechanical power  $P_{\text{Mech.,RMS}}$ , fluid power  $P_{\text{Fluid,RMS}}$ , or both, of our experimental and numerical results, compared with results of similar studies in the literature. The fluid power  $P_{\text{Fluid,RMS}}$  is calculated only from the results of our numerical study as the others did not measure lift. The computation of the instantaneous phase lag  $\phi$  requires both lift and cylinder displacement signals.

461 cylinder, thus creating a relative pistoning motion against a fixed magnet and produces an alternating current.

462 The estimated power in the KVIV regime  $U^* \leq 15.9$  produces power only in the order of  $\mu\text{W}$ , which is relatively  
 463 insignificant in contrast to the magnitude of power produced in the SVIV regime ( $\text{mW}$ ). In the region  $18.2 \leq U^* \leq 22.7$ ,  
 464  $P_{\text{Mech.,RMS}}$  for our experiment and numerical work exhibits a similar trend where we observed a sudden jump in power  
 465 output, followed by a gradual decrease. This gradual decrease can be attributed to the increased turbulence level right  
 466 after the onset of SVIV that imposes a degree of intermittency to the normalised cylinder displacement signal,  $y^*$ . For  
 467  $P_{\text{Fluid,RMS}}$ , however, the quantity exhibits a monotonic increase in the range  $18.2 \leq U^* \leq 22.7$ . We only observe  
 468 a dip in  $P_{\text{Fluid,RMS}}$  at  $U^* = 25.0$ , suggesting an increase in intermittency of  $C_{\text{Cl},y^*}$  at this  $U^*$ . In the experimental  
 469 work of Nguyen et al. (2012),  $P_{\text{Mech.,RMS}}$  only experiences a monotonic increase in the region  $18.2 \leq U^* \leq 22.7$ . This  
 470 decidedly different response of the system compared to ours most likely stem from the difference in the actual cruciform  
 471 used by Nguyen et al. (2012). They used two circular cylinders of diameter 10 mm as their cruciform, whereas we used  
 472 a circular cylinder - strip plate in both our experiments and numerical work. There are no data from the direct power  
 473 measurement of Koide et al. (2013) to compare with within  $18.2 \leq U^* \leq 22.7$ .

474 In the range  $25.0 \leq U^* \leq 29.5$ , we find a reasonably good agreement between the trend found in all data compared:  
 475 they increase monotonically with respect to  $U^*$ . Although the value of our  $P_{\text{Fluid,RMS}}$  falls quite notably below the value  
 476 of  $P_{\text{Mech.,RMS}}$  at  $U^* = 25.0$ , other values of  $P_{\text{Fluid,RMS}}$ ,  $P_{\text{Mech.,RMS}}$  from our numerical results and the direct power  
 477 measurements by Koide et al. (2013) agree well within  $27.3 \leq U^* \leq 29.5$ . The only set of power data that consistently  
 478 falls quite a distance below the others is the  $P_{\text{Mech.,RMS}}$  estimated from the experimental data of Nguyen et al. (2012),  
 479 which again, is most probably due to the difference in the actual geometry of the cruciform used in their investigation.

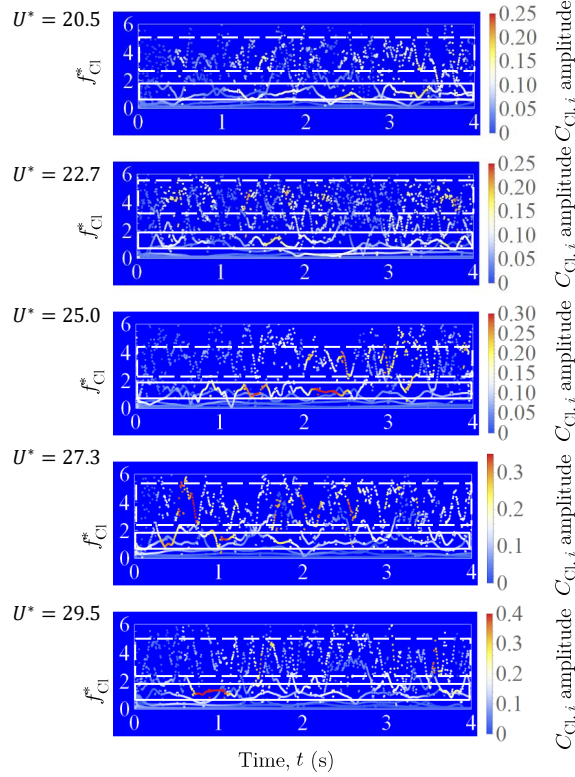


**Figure 21:** The instantaneous frequency of the lift signal between  $20.5 \leq U^* \leq 29.5$ . The white, solid boxes enclose the IMF component of CI due to the shedding of the streamwise vortex, while the dashed, white boxes enclose the IMF component due to the shedding of Karman vortex. Through visual inspection, we can see how the degree of dispersion (i.e., height of the box) in the instantaneous frequency of the “Karman component” of lift is about twice that of the “streamwise component” of lift.

## 480 6.2. Possibility for increasing fluid power, $P_{\text{Fluid,RMS}}$

481 Recall in Fig. 20 that although  $P_{\text{Fluid,RMS}}$  is computed according to Eq. 25, which uses  $C_{\text{Cl,RMS}}$  instead of the  
 482 actual root-mean-square amplitude of lift ( $\text{Cl}_{\text{RMS}}$ ), the resulting power estimate does not result in a trend that is totally  
 483 different from the trend found in the other datasets. Furthermore, except for  $P_{\text{Mech.,RMS}}$  estimated from the experimental  
 484 data of Nguyen et al. (2012), the values of  $P_{\text{Fluid,RMS}}$  are in fairly good agreement with other data that it is compared  
 485 against at high  $U^*$  ( $U^* = 27.3$  and  $29.5$ ). We see this is an indication that the lift component selected for use in  
 486 computation of  $P_{\text{Fluid,RMS}}$  is an arguably faithful representation of the force driving the motion of the cylinder. This  
 487 suggests that the motion of the cylinder, once it enters the SVIV regime, is driven only by one component of, and not  
 488 the totality of the lift force. This component – that has a time-averaged frequency close to the natural frequency of the  
 489 system,  $f_n$  – is the “streamwise component” of lift.

490 Another significant IMF component of the lift force in the SVIV regime is the component whose mean frequency  
 491 is close to the Karman frequency of vortex shedding, as explained in §5.3. This Karman component of lift has a similar  
 492 amplitude size as the streamwise component of lift, as evidenced in Fig. 21, and as such is also a dominant component

- Karman component ■ Streamwise component

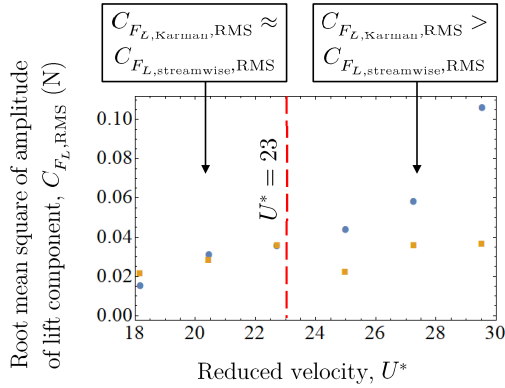


**Figure 22:** Evolution of the root-mean-square amplitude of two dominant lift components due to Karman ( $C_{F_L,Karman,RMS}$ ) and streamwise ( $C_{F_L,streamwise,RMS}$ ) vortices with respect to  $U^*$ . The region  $U^* \leq 22.7$  exhibits similar magnitude for both the Karman and streamwise components of lift. On the other hand, the magnitude of amplitude for the Karman component while the region  $U^* \geq 25.0$  is almost always twice that of the streamwise component.

of lift. The Karman components are marked with a dashed, white box, and the streamwise components are marked with a solid, white box, following the convention in Figs. 12, 13, 14, 16 and 17. However, the Karman component fails to affect the cylinder vibration like the streamwise component most probably due to the large difference between the mean frequency of the Karman component and the natural frequency of the system,  $f_n$ . The streamwise component has a mean frequency close to  $f_n$  and is hence able to synchronise with the vibration of the cylinder, producing a sizeable amplitude response.

Figure 22 shows the root-mean-square amplitude of the Karman and streamwise components of lift in the SVIV regime  $U^* \geq 18.2$ . Between  $18.2 \leq U^* \leq 22.7$ , the magnitude of the Karman and streamwise components are nearly equal. However, once we exceed  $U^* = 22.7$ , Fig. 22 shows that the contribution to the root-mean-square amplitude of total lift by the Karman component is on average twice the contribution of the streamwise component. Having such a significant contribution towards the root-mean-square amplitude of total lift implies that there is a significant portion of energy from the free stream being used to energise the Karman vortex structure in the flow. Let us assume a hypothetical situation where we can transfer the contribution by the Karman component to the streamwise component of lift. In other words, consider the situation where we can completely redirect the energy from the Karman to the streamwise vortex. Then, the value for  $C_{Cl,RMS}$  in Eq. 25 will increase close to a factor of 2 when  $18.2 \leq U^* \leq 22.7$ , and close to a factor of 3 when  $25.0 \leq U^* \leq 29.5$ . This increase in  $C_{Cl,RMS}$  will lead to the scaling of  $P_{Fluid,RMS}$  by the same factor, keeping the other parameters in Eq. 25 constant. This exercise demonstrates the room for improvement possible for  $P_{Fluid,RMS}$  in future developments of cruciform energy harvesters. We shall detail in our future work, a method to modulate the dominant vortical structures to achieve such a goal.

## 512 7. Conclusions

513 In this study, we numerically investigated the temporal evolution of the lift coefficient and cylinder displacement  
 514 signals of an elastically supported cruciform system in the range  $1.1 \times 10^3 < \text{Re} < 14.6 \times 10^3$ , or  $2.3 < U^* < 29.5$ .  
 515 Our circular cylinder diameter is 10 mm and the natural frequency of the system is 4.4 Hz. Validation of key numerical  
 516 results was made experimentally in a custom-built open flow channel, using a cruciform system whose parameters  
 517 were tuned as close as possible to the quantities used in the numerical study. Decomposing the lift coefficient signal in  
 518 the SVIV regime ( $15.9 \leq U^* \leq 29.5$ ) using EEMD allows us to see that the complexity of the lift coefficient signal as  
 519 being caused by the superpositioning of two dominant components of lift. One due to the shedding of Karman and the  
 520 other due to the shedding of streamwise vortices. The former has a frequency close to the vortex shedding frequency of  
 521 Karman vortex from a smooth, isolated circular cylinder, while the latter has a mean frequency close to  $f_n$ . Application  
 522 of the Hilbert-Huang transform on the dominant component of cylinder displacement – and the component of lift most  
 523 correlated to it – allows for the computation of the instantaneous phase lag between lift and cylinder displacement.  
 524 The time-averaged phase lag revealed five “branches” of vibration, among which is the initial branch of SVIV at  
 525  $U^* = 18.2$ , which has never been identified before in the literature. We also computed the instantaneous frequency of  
 526 the lift coefficient, thus revealing the loss of periodicity and self-similarity in the lift coefficient signal as the system  
 527 enters the SVIV regime. Estimation of power from our results show that the root-mean-square mechanical and fluid  
 528 power computed from our experimental and numerical work agree to varying degrees depending on  $U^*$  with data  
 529 from similar studies in the literature. Finally, we estimated that the root-mean-square fluid power can potentially be  
 530 increased close to a factor of 2 within  $18.2 \leq U^* \leq 22.7$  and close to a factor of 3 when  $25.0 \leq U^* \leq 29.5$ . We  
 531 base this estimation on the premise of redirecting the contribution to the root-mean-square amplitude of total lift from  
 532 Karman vortex shedding, towards the streamwise component of lift alone.

## 533 CRediT authorship contribution statement

534 **Ahmad Adzlan:** Conceptualisation of this study, Methodology, Software, Validation, Formal analysis, Investiga-  
 535 tion, Data curation, Writing - Original draft preparation, Visualisation. **Mohamed Sukri Mat Ali:** Conceptualisation  
 536 of this study, Methodology, Resources, Writing - Review & Editing, Supervision, Project administration, Funding  
 537 acquisition. **Sheikh Ahmad Zaki Shaikh Salim:** Resources, Writing - Review & Editing.

## 538 References

- 539 Ali, M.S.M., Doolan, C.J., Wheatley, V., 2012. Low Reynolds number flow over a square cylinder with a detached flat plate. International  
 540 Journal of Heat and Fluid Flow 36, 133–141. URL: <http://dx.doi.org/10.1016/j.ijheatfluidflow.2012.03.011>, doi:10.1016/j.ijheatfluidflow.2012.03.011.

## Lift Evolution in a Pure Cruciform Energy Harvester

- 542 Bernitsas, M., Raghavan, K., 2008. Reduction/suppression of VIV of circular cylinders through roughness distribution at  $8 \times 10^3 < Re < 1.5 \times 10^5$ ,  
543 in: Proceedings of the International Conference on Offshore Mechanics and Arctic Engineering - OMAE.
- 544 Bernitsas, M.M., Ben-Simon, Y., Raghavan, K., Garcia, E.M.H., 2009. The VIVACE Converter: Model Tests at High Damping and  
545 Reynolds Number Around  $10^5$ . Journal of Offshore Mechanics and Arctic Engineering 131. URL: <http://offshoremecanics.asmedigitalcollection.asme.org/article.aspx?articleid=1472649>, doi:10.1115/1.2979796.
- 546
- 547 Bernitsas, M.M., Raghavan, K., Ben-Simon, Y., Garcia, E.M.H., 2008. VIVACE (Vortex Induced Vibration Aquatic Clean Energy): A New  
548 Concept in Generation of Clean and Renewable Energy From Fluid Flow. Journal of Offshore Mechanics and Arctic Engineering 130,  
549 041101. URL: <http://www.scopus.com/record/display.url?eid=2-s2.0-56749179917&origin=resultslist&sort=plf-f&src=s&st1=A+new+concept+in+generation+of+clean+and+renewable+energy+from+fluid+flow&sid=620865A71FAF26768C42655E1E8BC194.aXczxbyuHHiXgaIW6Ho7g:230&sot=b&sdt=b&h>, doi:10.1115/1.2957913.
- 550
- 551
- 552 Blevins, R.D., 1990. Flow-induced vibration .
- 553 Deng, J., Ren, A.L., Shao, X.M., 2007. The flow between a stationary cylinder and a downstream elastic cylinder in cruciform arrangement.  
554 Journal of Fluids and Structures 23, 715–731. URL: <https://www.sciencedirect.com/science/article/pii/S0889974606001472>,  
555 doi:10.1016/J.JFLUIDSTRUCTS.2006.11.005.
- 556 Ding, L., Bernitsas, M.M., Kim, E.S., 2013. 2-D URANS vs. experiments of flow induced motions of two circular cylinders in tandem with  
557 passive turbulence control for 30,000. Ocean Engineering 72, 429–440. URL: <http://www.sciencedirect.com/science/article/pii/S0029801813002448?via%23Dihub>, doi:10.1016/J.OCEANENG.2013.06.005.
- 558
- 559 Ding, L., Zhang, L., Kim, E.S., Bernitsas, M.M., 2015a. URANS vs. experiments of flow induced motions of multiple circular cylinders with  
560 passive turbulence control. Journal of Fluids and Structures 54, 612–628. doi:10.1016/j.jfluidstructs.2015.01.003.
- 561 Ding, L., Zhang, L., Wu, C., Mao, X., Jiang, D., 2015b. Flow induced motion and energy harvesting of bluff bodies with different cross sections.  
562 Energy Conversion and Management doi:10.1016/j.enconman.2014.12.039.
- 563 Ding, W., Sun, H., Xu, W., Bernitsas, M.M., 2019. Numerical investigation on interactive FIO of two-tandem cylinders for hydrokinetic energy  
564 harnessing. Ocean Engineering 187, 106215. URL: <https://www.sciencedirect.com/science/article/pii/S0029801819304019>,  
565 doi:10.1016/J.OCEANENG.2019.106215.
- 566 Gumelar, A.B., Purnomo, M.H., Yuniarso, E.M., Sugiarto, I., 2019. Spectral Analysis of Familiar Human Voice Based On Hilbert-Huang Transform,  
567 in: 2018 International Conference on Computer Engineering, Network and Intelligent Multimedia, CENIM 2018 - Proceeding. doi:10.1109/CENIM.2018.8710943.
- 568
- 569 Huang, N.E., 2014. Hilbert-Huang transform and its applications. volume 16. World Scientific.
- 570 Huang, N.E., Attoh-Okine, N.O., 2005. The Hilbert-Huang transform in engineering. CRC Press.
- 571 Huang, N.E., Shen, Z., Long, S.R., Wu, M.C., Srin, H.H., Zheng, Q., Yen, N.C., Tung, C.C., Liu, H.H., 1998. The empirical mode decomposition  
572 and the Hubert spectrum for nonlinear and non-stationary time series analysis. Proceedings of the Royal Society A: Mathematical, Physical and  
573 Engineering Sciences doi:10.1098/rspa.1998.0193.
- 574 Kawabata, Y., Takahashi, T., Haginoya, T., Shirakashi, M., 2013. Interference Effect of Downstream Strip-Plate on the Crossflow Vibration of a  
575 Square Cylinder. Journal of Fluid Science and Technology 8, 647–658. doi:10.1299/jfst.8.348.
- 576 Khalak, A., Williamson, C., 1999. Motions, Forces And Mode Transitions In Vortex-Induced Vibrations At Low Mass-Damping. Journal of Fluids  
577 and Structures 13, 813–851. URL: <http://www.sciencedirect.com/science/article/pii/S0889974699902360>, doi:10.1006/jfls.1999.0236.
- 578
- 579 Koide, M., Kato, N., Yamada, S., Kawabata, Y., Takahashi, T., Shirakashi, M., 2007. Influence Of A Cruciform Arrangement Downstream Strip-

## Lift Evolution in a Pure Cruciform Energy Harvester

- 580 Plate On Crossflow Vibration. Journal of Computational and Applied Mechanics 8, 135–148.
- 581 Koide, M., Ootani, K., Yamada, S., Takahashi, T., Shirakashi, M., 2006. Vortex Excitation Caused by Longitudinal Vortices Shedding from  
582 Cruciform Cylinder System in Water Flow. JSME International Journal 49, 1043–1048.
- 583 Koide, M., Sekizaki, T., Yamada, S., Takahashi, T., Shirakashi, M., 2009. A Novel Technique for Hydroelectricity Utilizing Vortex Induced  
584 Vibration, in: Proceedings of the ASME Pressure Vessels and Piping Division Conference, PVP2009-77487.
- 585 Koide, M., Sekizaki, T., Yamada, S., Takahashi, T., Shirakashi, M., 2013. Prospect of Micro Power Generation Utilizing VIV in Small  
586 Stream Based on Verification Experiments of Power Generation in Water Tunnel. Journal of Fluid Science and Technology 8, 294–  
587 308. URL: [https://www.jstage.jst.go.jp/article/jfst/8/3/8{\\_}294/{}articlehttp://jlc.jst.go.jp/DN/JST.JSTAGE/](https://www.jstage.jst.go.jp/article/jfst/8/3/8{_}294/{}articlehttp://jlc.jst.go.jp/DN/JST.JSTAGE/)  
588 jfst/8.294?lang=en&from=CrossRef&type=abstract, doi:10.1299/jfst.8.294.
- 589 Koide, M., Takahashi, T., Shirakashi, M., Salim, S.A.Z.B.S., 2017. Three-dimensional structure of longitudinal vortices shedding from cruciform  
590 two-cylinder systems with different geometries. Journal of Visualization , 1–11.
- 591 Langley Research Centre, 2018. Turbulence Modeling Resource. URL: <https://turbmodels.larc.nasa.gov/>.
- 592 Maruai, N.M., Ali, M.S.M., Ismail, M.H., Zaki, S.A., 2018. Flow-induced vibration of a square cylinder and downstream  
593 flat plate associated with micro-scale energy harvester. Journal of Wind Engineering and Industrial Aerodynamics 175, 264–  
594 282. URL: [https://www.scopus.com/inward/record.uri?eid=2-s2.0-85042219159&doi=10.1016%2Fj.jweia.2018.01.010](https://www.scopus.com/inward/record.uri?eid=2-s2.0-85042219159&doi=10.1016%2Fj.jweia.2018.01.010&partnerID=40&md5=2f3f62b94bb69ced3368b32e682aefc7).
- 595 Maruai, N.M., Mat Ali, M.S., Ismail, M.H., Shaikh Salim, S.A.Z., 2017. Downstream flat plate as the flow-induced vibration enhancer for energy har-  
596 vesting. Journal of Vibration and Control , 107754631770787URL: <http://journals.sagepub.com/doi/10.1177/1077546317707877>,  
597 doi:10.1177/1077546317707877.
- 598 Mat Ali, M.S., Doolan, C.J., Wheatley, V., 2011. Low Reynolds number flow over a square cylinder with a splitter plate. Physics of Fluids 23.  
599 doi:10.1063/1.3563619.
- 600 Nguyen, T., Koide, M., Yamada, S., Takahashi, T., Shirakashi, M., 2012. Influence of mass and damping ratios on VIVs of a cylinder with a  
601 downstream counterpart in cruciform arrangement. Journal of Fluids and Structures 28, 40–55. doi:10.1016/j.jfluidstructs.2011.10.  
602 006.
- 603 Raghavan, K., 2007. Energy Extraction from a Steady Flow Using Vortex Induced Vibration. Doctoral dissertation. The University of Michigan.  
604 URL: <http://deepblue.lib.umich.edu/handle/2027.42/55687>.
- 605 Raghavan, U., Albert, R., Kumara, S., 2007. Near linear time algorithm to detect community structures in large-scale networks. Phys. Rev E. 76,  
606 036106.
- 607 Richardson, L.F., Gaunt, J.A., 1927. The deferred approach to the limit. Philosophical Transactions of the Royal Society A doi:<https://doi.org/10.1098/rsta.1927.0008>.
- 608 Shirakashi, M., Mizuguchi, K., Bae, H.M., 1989. Flow-induced excitation of an elastically-supported cylinder caused by another located downstream  
609 in cruciform arrangement. Journal of Fluids and Structures 3, 595–607. doi:10.1016/S0889-9746(89)90150-3.
- 610 Stern, F., Wilson, R.V., Coleman, H.W., Paterson, E.G., 2001. Comprehensive approach to verification and validation of CFD simulationsii;part 1:  
611 methodology and procedures. Journal of fluids engineering 123, 793–802.
- 612 Sun, H., Kim, E.S., Nowakowski, G., Mauer, E., Bernitsas, M.M., 2016. Effect of mass-ratio, damping, and stiffness on optimal hydrokinetic energy  
613 conversion of a single, rough cylinder in flow induced motions. Renewable Energy 99, 936–959. URL: <http://www.sciencedirect.com/science/article/pii/S0960148116306206>, doi:10.1016/j.renene.2016.07.024.
- 614 Wu, W., 2011. Two-Dimensional RANS Simulation of Flow Induced Motion of Circular Cylinder with Passive Turbulence Control. Doctoral  
615

## Lift Evolution in a Pure Cruciform Energy Harvester

- 618 dissertation. The University of Michigan.
- 619 Wu, Z., Huang, N.E., 2008. Ensemble Empirical Mode Decomposition: A Noise-Assisted Data Analysis Method. Advances in Adaptive Data  
620 Analysis doi:10.1142/s1793536909000047.
- 621 Zhang, B., Mao, Z., Song, B., Ding, W., Tian, W., 2018. Numerical investigation on effect of damping-ratio and mass-ratio on energy  
622 harnessing of a square cylinder in FIM. Energy 144, 218–231. URL: <https://www.scopus.com/inward/record.uri?eid=2-s2.0-85037995662&doi=10.1016%2Fj.energy.2017.11.153&partnerID=40&md5=01db7c6b6d4d44e88de7045843c7d423>,  
623 doi:10.1016/j.energy.2017.11.153.
- 624 Zhao, M., Lu, L., 2018. Numerical simulation of flow past two circular cylinders in cruciform arrangement. Journal of Fluid Mechanics 848, 1013–  
625 1039. URL: [https://www.cambridge.org/core/product/identifier/S0022112018003804/type/journal\\_article](https://www.cambridge.org/core/product/identifier/S0022112018003804/type/journal_article), doi:10.  
626 1017/jfm.2018.380.
- 627 Zhou, L., Meng, Y., Abbaspour, K.C., 2019. A new framework for multi-site stochastic rainfall generator based on empirical orthogonal function  
628 analysis and Hilbert-Huang transform. Journal of Hydrology doi:10.1016/j.jhydrol.2019.05.047.
- 629